PHYSICAL REVIEW E **95**, 022418 (2017)

Simple empirical model for identifying rheological properties of soft biological tissues

Yo Kobayashi[*]
Future Robotics Organization, Waseda University, Tokyo 169-8555, Japan; JST-PRESTO, Saitama 332-0012, Japan;
and Graduate School of Engineering Science, Osaka University, Osaka 560-8531, Japan

Mariko Tsukune, Tomoyuki Miyashita, and Masakatsu G. Fujie
Faculty of Science and Engineering/Research Institute of Science and Engineering, Waseda University, Tokyo 169-8555, Japan

(Received 7 September 2015; revised manuscript received 11 September 2016; published 28 February 2017)

Understanding the rheological properties of soft biological tissue is a key issue for mechanical systems used in the health care field. We propose a simple empirical model using fractional dynamics and exponential nonlinearity (FDEN) to identify the rheological properties of soft biological tissue. The model is derived from detailed material measurements using samples isolated from porcine liver. We conducted dynamic viscoelastic and creep tests on liver samples using a plate-plate rheometer. The experimental results indicated that biological tissue has specific properties: (i) power law increase in the storage elastic modulus and the loss elastic modulus of the same slope; (ii) power law compliance (gain) decrease and constant phase delay in the frequency domain; (iii) power law dependence between time and strain relationships in the time domain; and (iv) linear dependence in the low strain range and exponential law dependence in the high strain range between stress-strain relationships. Our simple FDEN model uses only three dependent parameters and represents the specific properties of soft biological tissue.

DOI: 10.1103/PhysRevE.95.022418

I. INTRODUCTION

A. Background

Understanding the physical phenomena underlying the mechanical properties of human tissue has a great impact on bioscience and engineering. This knowledge will lead to further development of machines and systems in the health care field. Recently, the health care field has realized the benefit of using intelligent machines (such as robots) that can physically interact with humans. As a by-product, the physical information measured by the machines can also be used for cybersystem construction (such as machine learning).

Understanding the rheology, the study of materials with both solid and fluid characteristics in which the response to strain under applied stress is evaluated, of biological tissues is a key issue for current research in the human health care field. Rheology is relevant to many technological applications, ranging from biological science (e.g., medicine, sports, biology, biomechanics) to engineering (e.g., robotics, mechatronics, material mechanics, control theory, computational mechanics, information technology). Modeling of soft tissue rheological properties is a core technology for developing various health care machines and systems to assist human activity. For example, a mathematical model of target objects (human, organ, tissue, etc.) is required for mechanical design, motion planning, information processing, and control.

These research and development areas require fundamental equations that are limited to the essential properties of the macroscopic behavior of the target matter (i.e., microscale modeling is not necessary). In short, the development of fundamental macroscopic models of the properties of biological matter is a key research issue pertinent to health care machines and systems designed for humans, organs, and tissues.

In spite of their scientific and technological importance, mainly because they are difficult to model, very little knowledge has been established regarding the rheological properties of soft biological tissues. The properties of soft biological tissues are different from those of synthetic matter, and the rheological properties of soft biological tissue cannot be directly modeled in the same manner as synthetic matter [1,2]. This difference in properties has limited the development of methods for sensing, parameterizing and information processing of rheological properties of soft biological tissue.

B. Goal and motivation

The goal of this study is to establish a universal fundamental model to represent the macroscopic rheological properties of soft biological tissue, as well as a method for measuring these properties.

The motivation behind this study is the need for a “simple model” that accurately represents the specific rheological properties of soft biological tissue. The model should be strongly correlated with experimental data derived from actual biological tissue. A “simple model” means that the model should utilize the minimum number of parameters, yielding a mathematical equation that is easy to understand and implement. Use of a simple model is essential for robust identification and discrimination of tissues using rheological information.

C. Related research

Many researchers have reported that the rheological properties of soft biological tissues have distinct properties in comparison to industrial synthetic materials [1,3], such as metals. For example, researchers reported that biological tissues have viscoelastic properties [1–4]. Researchers have also reported that soft biological tissues exhibit a very nonlinear relationship between strain and stress [1–7]. Numerous studies have dealt with both the nonlinearity and/or viscoelasticity of biological tissue [1–31]. Models that neglect viscoelasticity and/or

---

[*] you-k@fuji.waseda.jp

nonlinearity result in variability and incongruous analysis of the rheological properties of soft biological tissue [1,3,10]. In this article, we describe the complex viscoelastic and nonlinear properties of soft biological tissue as "rheological properties."

An ordinary linear differential equation (LDE) is generally used to model viscoelastic properties (e.g., Voigt-Maxwell-Kelvin model) [1–4]. In other words, the terms of the equation for rheological properties have been generally modeled using both "linear" and "integer order" differential equations explicitly or implicitly. Small order LDE models do not fit data from biological tissues well, and a large number of parameters are used in LDEs to increase model accuracy (e.g., generalized Maxwell model). These models only represent linear relationships between stress and strain [1,3,6,8,9].

Hyperelastic models (e.g., Ogden, Mooney-Rivlin models) are generally used to represent stress-strain nonlinearity [1–7], although the number of parameters in hyperelastic models also tends to be large. Moreover, these models are time independent and do not represent dynamic (viscoelastic) properties. Thus, additional terms and parameters are needed to represent dynamic properties in a hyperelastic model [10].

The equations in some related work [4,6,21–31] have dealt with both viscoelasticity and nonlinearity. However, these models tend to become overly complex and involve an excess number of material parameters to represent these properties. Existing models with numerous parameters, such as those combining hyperelastic models with viscoelastic models, are unsuitable for identifying model parameters. The use of a large number of parameters leads to a risk of overfitting the parameter identification and ill-posedness of inverse problems. Having a large number of parameters also increases computational costs.

A standard model based on a simple equation with few parameters that is highly correlated with experimental data from soft biological tissues does not currently exist. A preferred model should have a small number of parameters that are strongly correlated with the experimental data. Therefore, we have conducted studies aimed at developing a model with these characteristics [32–39]. The model is derived from comprehensive material data obtained from *in vitro* measurements of porcine liver [32–35]. The model was also validated using *in vitro* breast tissue (fibroglandular tissue, fat, muscle) [36,37] and partially evaluated using muscle tissue [38,39]. The model combines a fractional differential equation with a polynomial expression for stress-strain nonlinearity, which consists of four parameters [32–37]. However, two parameters in the model, both parameters representing nonlinear properties, correlate and interfere with one another. In addition, the parameter identification from the experimental data of these two parameters is complex; specifically, global searching and optimization are required. Moreover, the physical laws of soft biological tissue were not explicitly introduced in these articles. The model and scope of these earlier publications are briefly introduced in Appendix A.

D. Objectives

The objective of this article is to propose a simple model that represents the rheological properties, meaning, viscoelastic and nonlinear properties, of soft biological tissues. Specifically, we propose a simple model, using only three dependent parameters, incorporating fractional dynamics and exponential nonlinearity to identify rheological properties. The advantage of our model is that it is strongly correlated with various experimental data and uses a small number of parameters, thereby rendering it suitable for parameter identification and inverse analysis. This article also examines the physical laws of soft biological tissue based on the experimental data and model.

Figure 1 shows an overview of this article. The model is derived from detailed material measurements using actual biological tissue. Specifically, we used samples isolated from various porcine livers. We selected liver samples because liver is a relatively simple tissue with low anisotropy when compared with other biological organs and tissues. We used a plate-plate rheometer to measure the liver samples, as the rheometer can dynamically control and measure stress and strain applied to the sample. We conducted a dynamic viscoelastic test and creep test to derive and evaluate the model. Individual differences between liver samples (physical properties of biological tissues differ between individual samples) were represented by the values of model parameters.

II. MATERIALS AND METHODS

In this section, we explain how we measured and modeled the rheological properties of the samples. First, we introduce our rheological model scheme. We then explain the study materials and measurement procedures.

A. Proposed model

The rheological model in this study relies on experimental data obtained from biological tissues. We first give the model equations (1a) and (1b) to enhance the readability of this article. Here, we present a scalar and simple shear model for soft biological tissue. The proposed rheological model utilizes fractional dynamics and exponential nonlinearity (FDEN); the equations are as follows:

$$t_r^\alpha \frac{d^\alpha}{dt^\alpha}(Gx) = f \quad \{x < x_b\}, \tag{1a}$$

$$t_r^\alpha \frac{d^\alpha}{dt^\alpha}\left(Gx_b e^{\frac{x-x_b}{x_b}}\right) = f \quad \{x > x_b\}, \tag{1b}$$

where x is strain (torsional strain), f is stress (torsional stress), and t is time, as variables; α is a noninteger derivative order representing the index of viscoelasticity, t_r is the reference time scale, G is the linear viscoelastic stiffness at an arbitrarily chosen time t_r, and x_b is the boundary strain in which the characteristics change to nonlinearity, as the parameters of the model. e is Napier's constant. The details of the calculations regarding x and f are described in Appendix B.

Equation (1b) is derived from the connectivity between linear equation (1a) and exponential nonlinear equation (1b); the exponential curve (1b) is tangent to the straight line (1a).

The other form of Eq. (1b) is as follows:

$$t_r^\alpha \frac{d^\alpha}{dt^\alpha}(G_i e^{G_n x}) = f \quad \{x > 1/G_n\} \tag{2}$$

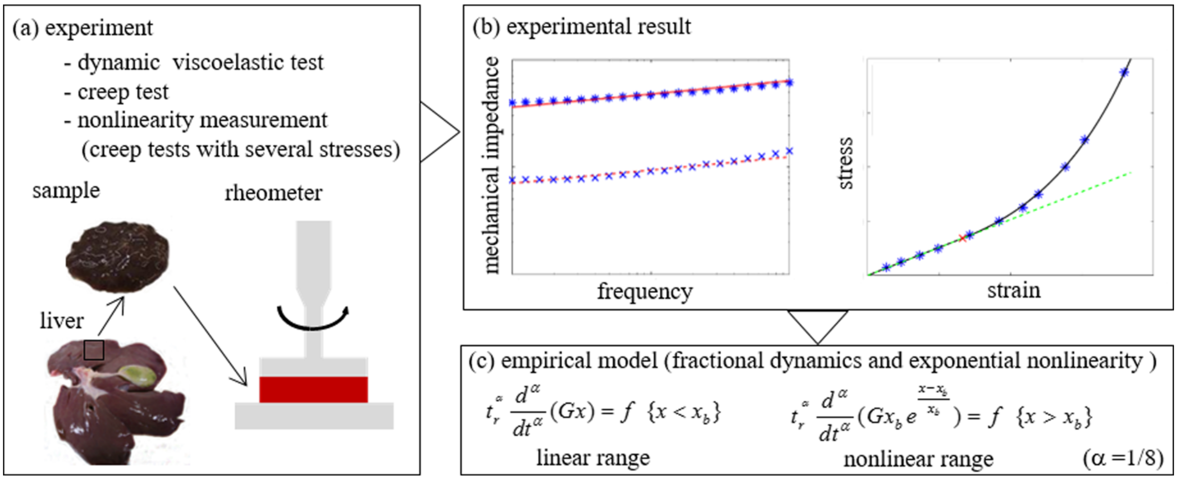

FIG. 1. An overview of this article. The model is derived from detailed material measurements using actual biological tissue. Specifically, we used samples isolated from various porcine livers. We used a plate-plate rheometer to measure the liver samples in which the rheometer can dynamically control and measure stress and strain applied to the sample (a). For example, we conducted a dynamic viscoelastic test and a creep test with several stresses (b) to derive and evaluate our empirical model (c). Individual differences between liver samples (physical properties of biological tissues differ between individual samples) were represented by the values of model parameters.

where G_n is nonlinear viscoelastic stiffness (G_i is a dependent parameter). Each parameter should fulfill the following relationship (3) concerning the connectivity between (1a) and (2). The detailed calculation is described in Appendix E:

$$G_n = \frac{1}{x_b}, \quad G_i = \frac{Gx_b}{e}. \tag{3}$$

The model has a total of three parameters, α, G, and G_n (or $\boldsymbol{x_b}$), as representative parameters according to the relationships in (3).

The details of the experimental methods and derivation process of the model from the experimental data are described in the next sections.

B. Materials and conditions

Figure 2 shows the details of the measuring components. We used porcine liver in this study because porcine abdominal organs have properties similar to those of humans and are widely used in laparoscopic surgery training for novice surgeons. We chose to measure the properties of liver samples because liver, consisting of homogeneous and isotropic tissue, would be relatively easy to model. We used cryogenically preserved liver samples (4 °C on ice) that were taken within 24 h postmortem and that did not include membranes or large blood vessels. Specimens were not frozen at any time during the procedure.

We used a plate-plate rheometer (AR550 or AR-G2; TA Instruments, New Castle, DE) to measure the stress loaded on the sample and sample strain. The shear stress rheometer was selected because the shear test must be independent of any change in cross-sectional area in the stress calculation. In addition, the effect of gravity could be disregarded. From these measurements, the conventional shear strain x and conventional shear stress f were calculated. The measurements of strain x and stress f are valid only when there is no slip between the sample and the plates. Thus, sandpaper (P80 grain size) was attached to the top plate and the measurement table to prevent sliding. The details of the calculation are described in Appendix B. The liver sample was cut into slices (diameter 20 mm, height 5 mm), and the slices were placed on a measurement table. The samples were soaked in saline solution at 35 °C during each test.

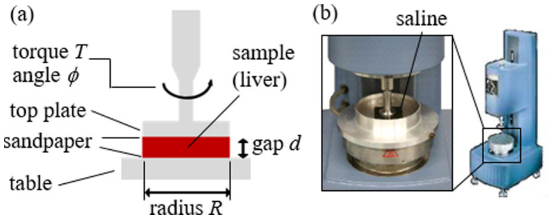

FIG. 2. Details of the measuring components (a) and actual experimental setup (b). We used porcine liver as the sample for this study. We used a plate-plate rheometer to measure the stress loaded on the sample and sample strain. The liver sample was cut into slices, and the slices were placed on a measurement table. The samples were soaked in a saline solution at 35 °C during each test. Sandpaper was attached to the top plate and the measurement table to prevent sliding. Radius R was 20 mm and gap d was 5 mm.

C. Procedures

1. Initializing procedures

After the saline solution reached the target temperature, the gap was zeroed to the surface of the saucer. The saline solution was stable and there was no reflux flow. Each tissue sample was placed on a measurement table, and the sample thickness (=gap d) was determined. The sample thickness was defined as the distance between the surface of the saucer and the surface of the parallel plate (part of the measuring device) at the time that the normal stress resulting from contact between the parallel plate and the sample reached 0.1 N. To engage the sample and parallel plate, preloading for 180 s and unloading for 180 s were performed thrice under a load constant shear stress f_c of

750 Pa. The following series of experiments were conducted for each sample, after the above initializing procedures.

2. Dynamic viscoelastic test

Sine-wave stress from 0.1 to 10 rad/s, providing 1.5% strain amplitude x_o, was applied to the sample. The compliance J (gain from stress amplitude f_o to strain amplitude x_o), phase delay ϕ, storage elastic modulus G', and loss elastic modulus G'' of each angular frequency ω were measured. As shown in the following experimental results (Fig. 6), 1.5% (=0.015) strain amplitude is in the range where liver tissue exhibits linear responses. The effect of mass (inertia) and shear viscosity from the external normal saline solution could be disregarded at frequencies less than 10 rad/s. Data were collected from 11 liver samples. We obtained a pair of results (storage elastic modulus G', loss elastic modulus G'') or (compliance J, phase ϕ) from the dynamic viscoelastic test. The detailed process to obtain the experimental results from the dynamic viscoelastic test is provided in Appendix C.

3. Creep test and nonlinear measurement

A torsional creep test was performed after the dynamic viscoelastic test. The creep test, in which step responses to strain $x(t)$ are observed under constant stress f_c, was repeatedly performed, applying several stresses on the sample. Time series of strain data $x(t)$ were measured during each experiment. The constant shear stress f_c load ranged from 25 to 750 Pa, and the time series of strain data $x(t)$ were recorded for 180 s at each stress level. Each test was performed at intervals of 180 s. The load shear stress during each interval was 0 Pa. The reference strain was set to 0 at each creep test to account for residual stress and strain. We ignored the data obtained from 0 to 1 s because of vibrations during the early transient stage. The details of this area are presented in our previous article [34,35]. Data were collected from 64 liver samples.

III. RESULTS AND MODELING

A. Mechanical complex impedance

Here, mechanical complex impedance G^* is defined as follows:

$$G^*(\omega) = G'(\omega) + jG''(\omega). \tag{4}$$

Here, ω is angular frequency, j is the imaginary unit, G^* is the complex mechanical impedance, G' is the storage elastic modulus, and G'' is the loss elastic modulus.

Typical experimental results of a dynamic viscoelastic test (in this section, mechanical complex impedance G^*) of a sample are shown in Fig. 3. All liver samples exhibit the same trend as the typical sample; data trends are the same, however, model fit data and parameters are different.

Both the storage elastic modulus G' and the loss elastic modulus G'' increased with the angular frequency ω. We found that both the storage elastic modulus G' and the loss elastic modulus G'' exhibit a power law form over two decades. Furthermore, G' and G'' are approximately proportional to $\omega^{1/8}$ ($\alpha = 0.125 = \frac{1}{8}$).

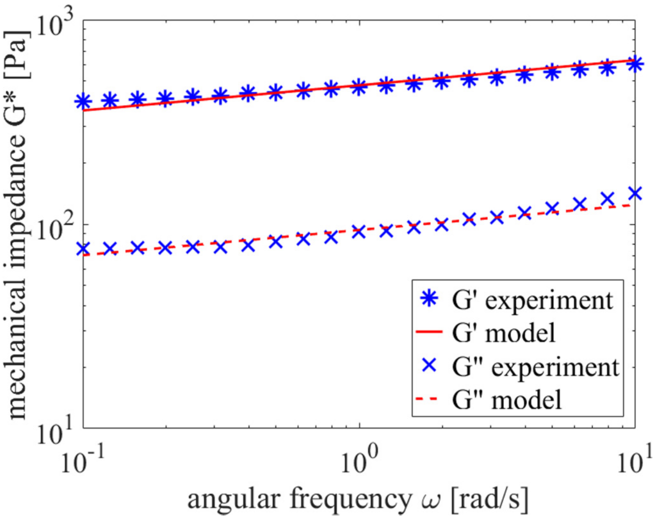

FIG. 3. Mechanical complex impedance. The typical experimental results of a dynamic viscoelastic test (in this figure, mechanical complex impedance) of a sample. The asterisk plot is the experimental result for the storage elastic modulus G'. The cross plot is the experimental result for the loss elastic modulus G''. Both the storage elastic modulus G' and the loss elastic modulus G'' increased as the angular frequency ω increased. Both the storage elastic modulus G' and the loss elastic modulus G'' exhibit a power law form over two decades. Furthermore, G' and G'' are approximately proportional to $\omega^{1/8}$ ($\alpha = 0.125 = \frac{1}{8}$). The G' of our model is the line, and the G'' of our model is the dashed line. The G' and G'' of our model, which fit the typical experimental results, indicate that our model and the experimental results are highly correlated.

The mechanical complex impedance of our model has the same characteristics as the experimental results, i.e., power law forms of G' and G'', and the same slopes of G' and G''. The expansion of the equation to explain the above characteristics is as follows. Our model is represented as Eq. (5) [the same equation as (1a) is described for readability] because the dynamic viscoelastic tests were conducted in the linear range of the stress-strain relationship

$$t_r^\alpha \frac{d^\alpha}{dt^\alpha}(Gx) = f. \tag{5}$$

Because Eq. (5) takes the form of a frequency transfer function, the complex shear modulus G^* can be expressed in terms of the Laplace operator as follows:

$$G^*(s) = \frac{F(s)}{X(s)} = G\,(t_r s)^\alpha. \tag{6}$$

Equation (7) is derived from the mechanical complex impedance of (6) using $s = j\omega$:

$$G^*(j\omega) = G\left(j\frac{\omega}{\omega_r}\right)^\alpha. \tag{7}$$

Here, ω is the angular frequency, ω_r is the reference scale, defined as $\omega_r = 1/t_r$. The reference scale ω_r is used in the following explanations about the frequency domain, Secs. III A and III B and Appendix F, to enhance the readability of this article.

TABLE I. Accuracy evaluation results for the present model.

Equation and experimental data	Sample number (number of trials)	Avg. of R^2	Max. of R^2	Min. of R^2	S.D. of R^2
Equations (11a) and (11b) and dynamic viscoelastic test	11	0.840	0.902	0.751	0.008
Equation (18) and creep results	64 (712)	0.997	1.000	0.950	0.0073
Equations (19a) and (19b) and nonlinear measurement	64	0.986	1.000	0.923	0.018

Then, Eq. (7) expands to (8a) and (8b) from (4) with separation of the real and imaginary parts of (7):

$$G'(\omega) = G'(\omega_r)\left(\frac{\omega}{\omega_r}\right)^{\alpha}, \tag{8a}$$

$$G''(\omega) = G''(\omega_r)\left(\frac{\omega}{\omega_r}\right)^{\alpha}. \tag{8b}$$

Here, $G'(\omega_r)$ is a constant parameter that represents the storage elastic modulus, and $G''(\omega_r)$ is a constant parameter that represents the loss elastic modulus. These parameters have the following relationship (10) because of a constant parameter that represents the complex modulus $G^*(j\omega_r)$ derived from (9):

$$G^*(j\omega_r) = G\,(j)^{\alpha} = G\cos\left(\frac{\pi}{2}\alpha\right) + jG\sin\left(\frac{\pi}{2}\alpha\right), \tag{9}$$

$$G = \sqrt{G'(\omega_r)^2 + G''(\omega_r)^2}, \tag{10a}$$

$$G'(\omega_r) = G\cos\left(\frac{\pi}{2}\alpha\right), \tag{10b}$$

$$G''(\omega_r) = G\sin\left(\frac{\pi}{2}\alpha\right). \tag{10c}$$

Equations (11a) and (11b) were derived from (8a) and (8b) by log-log transformation through the transformation to dimensionless quantities:

$$\log\left[\frac{G'(\omega)}{G'(\omega_r)}\right] = \alpha\log\left(\frac{\omega}{\omega_r}\right), \tag{11a}$$

$$\log\left[\frac{G''(\omega)}{G''(\omega_r)}\right] = \alpha\log\left(\frac{\omega}{\omega_r}\right). \tag{11b}$$

Thus, our model equation represents the same trend as the experimental results, i.e., power law dependence of G' and G''. The parameters (G and α) of Eqs. (11a) and (11b) were identified by fitting the experimental results for each sample. We used the extended Kalman filter (EKF) algorithm to identify the parameters (see Appendix F for details) because Eqs. (11a) and (11b) are nonlinear simultaneous equations: both equations include parameters (G and α). The G' and G'' in our model, which fit typical experimental results, are shown in Fig. 3, showing that our model and the experimental results are strongly correlated. It should be noted that the derivative order α is not an integer ($\alpha = 0.125 = \frac{1}{8}$). Our model also fits the experimental data from all liver samples well. The coefficient of determination R^2 between our model and the experimental data from the series of G' and G'' in all samples is approximately 90%. Each data set was fitted with a pair (G,α), and then the results were averaged. Tables I and II list the model accuracy evaluation and fundamental statistics of the model parameters. For example, the average data of (G,α) are shown in Tables I and II.

B. Bode diagram

Typical experimental results of a dynamic viscoelastic test (in this section, a gain diagram and phase diagram) of a sample are shown in Fig. 4. Figure 4 is a plot of the same data presented in Fig. 3, the only difference being the expression of data from dynamic viscoelastic tests. Compliance (gain) J, the multiplicative inverse of G^*, decreased as angular frequency ω increased. We found that compliance (gain) J assumes a power law form over two decades. We also found that the phase delay ϕ remained constant over two decades.

The Bode diagram of our model has the same characteristics as the experimental results, namely, power law form of compliance (gain) J and constant phase delay ϕ. The expansion of the equation to explain the above characteristics is as follows. The Laplace operator of the Bode diagram is as follows:

$$J(s) = \frac{X(s)}{F(s)} = \frac{1}{G(t_r s)^{\alpha}}, \tag{12a}$$

$$J(j\omega) = \frac{1}{G\left(j\frac{\omega}{\omega_r}\right)^{\alpha}}. \tag{12b}$$

TABLE II. Fundamental statistics of the parameters when $t_r = 1$ ($\omega_r = 1$).

Test	Parameter	Sample number	Avg.	Max.	Min.	S.D.
Dynamic viscoelastic test	G	11	391.1	518.2	248.2	111.2
Dynamic viscoelastic test	α	11	0.131	0.146	0.118	0.011
Dynamic viscoelastic test	J_o	11	0.00275	0.00402	0.00192	0.000853
Dynamic viscoelastic test	ϕ	11	−11.85	−10.60	−13.12	0.980
Nonlinearity measurement	G	64	544.8	1294	341.8	155.3
Nonlinearity measurement	G_n	64	8.547	13.18	5.26	1.604
Nonlinearity measurement	x_b	64	0.121	0.190	0.076	0.0022
Nonlinearity measurement	G_i	64	23.90	39.64	11.35	6.206

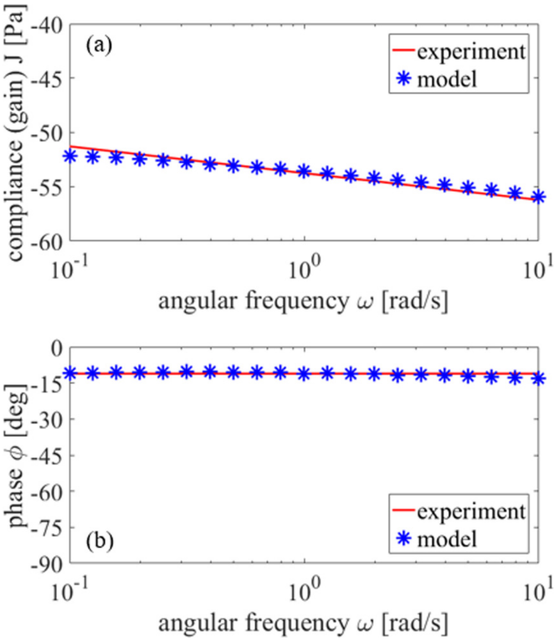

FIG. 4. Bode diagram. The typical experimental results of a dynamic viscoelastic test [gain diagram (a) and phase diagram (b)] of a sample. The plots in the gain diagram and phase diagram show the experimental results. Compliance (gain) J, the multiplicative inverse of G^*, decreased as the angular frequency ω increased. Compliance J assumes a power law form over two decades. We also found that the phase delay ϕ remained constant over two decades. The lines are the compliance (gain) J and phase ϕ results of our model. The parameters of our model fit the typical experimental results, showing that our model and the experimental results are highly correlated.

The compliance (gain) J is defined from Eq. (12) as follows:

$$J(\omega)=\left|\frac{1}{G\left(j\frac{\omega}{\omega_r}\right)^{\alpha}}\right|=\frac{1}{G\left(\frac{\omega}{\omega_r}\right)^{\alpha}}=\frac{J(\omega_r)}{\left(\frac{\omega}{\omega_r}\right)^{\alpha}}, \tag{13}$$

where $J(\omega_r)$ is the coefficient that represents the compliance, defined as $J(\omega_r)=J_o=1/G$.

Equation (14) is derived from the log-log transformation of (13) through the transformation to dimensionless quantities

$$\log\left[\frac{J(\omega)}{J(\omega_r)}\right]=-\alpha\log\left(\frac{\omega}{\omega_r}\right). \tag{14}$$

In addition, the model equation of the phase delay ϕ is derived from (8a) and (8b):

$$\phi(\omega)=\arg\left[\frac{1}{G\left(j\frac{\omega}{\omega_r}\right)^{\alpha}}\right]=-\frac{\pi}{2}\alpha=\phi_o, \tag{15}$$

where ϕ_o $(=-\frac{\pi}{2}\alpha)$ is the coefficient that represents the phase delay. Thus, our model equation represents the trend observed in the experimental results.

We calculated the compliance (gain) J and phase ϕ of our model via identification of the parameter of mechanical complex impedance for each sample because the parameters were the same. The compliance (gain) J and phase ϕ results from our model, the parameters of which fit the typical experimental results, are shown in Fig. 4, which shows that our model and the experimental results are strongly correlated. Our model fit the experimental data from all liver samples well. Each data set was fitted with a pair (J_o, ϕ_o), and then the results were averaged. Table II lists the fundamental statistics of the model parameters. For example, the average data of (J_o, ϕ_o) are shown in Tables I and II.

C. Creep test (step response)

A typical example of the experimental results for a creep test, the creep response obtained by assuming the input step stress, is shown in Fig. 5(a). The strain of liver samples increased over a time interval of 180 s. Figure 5(b) shows a log-log diagram of the same data described in Fig. 5(a). We found that the time series data of the creep response exhibited a power law form over two decades [Fig. 5(b)].

A model equation of strain $x(t)$ in the creep test can be calculated. We assumed that Eq. (1a) is valid for a single creep test, while nonlinearity was evaluated by a series of creep tests under several applied stresses f_c. Specifically, Eq. (1a) becomes (16) if (1a) is solved for the conditions of the creep test. Here, the applied stress is constant f_c.

Strictly and theoretically speaking, the quantity x_c is well defined by Eq. (16) at small deformations $x < x_b$ based on (1a), but is not defined at deformations $x > x_b$ based on (1b). However, we use here Eqs. (16) and (1a) also in the nonlinear range $x > x_b$ for a single creep test because the power law is still useful to determine the quantity x_c (the details of this point are explained in Appendix D):

$$x(t)=\frac{f_c}{G\Gamma(1+r)}\left(\frac{t}{t_r}\right)^{\alpha}=x_c\left(\frac{t}{t_r}\right)^{\alpha}. \tag{16}$$

Here, x is strain, t is time, f_c is constant applied stress, and $\Gamma(\ldots)$ is the gamma function. x_c is the coefficient determining the strain value as a parameter, which is defined as follows:

$$x_c=\frac{f_c}{G\Gamma(1+\alpha)}. \tag{17}$$

In this case, the Riemann-Liouville definition [40] (but not only this definition) was used to solve the fractional integration of (1a). Equation (18) is derived from the log-log transformation of (16) through the transformation to dimensionless quantities

$$\log\left(\frac{x}{x_c}\right)=\alpha\log\left(\frac{t}{t_r}\right). \tag{18}$$

Thus, our model equation represents the trend observed in the experimental results. The parameters (x_c, α) of Eq. (18) were identified by fitting the experimental results in the log-log domain. We used the least squares method (LSM) algorithm, linear regression, to identify the parameters of Eq. (18) for each sample. We calculated the other independent parameter G via Eq. (17). The time series data $x(t)$ from our model, the parameters of which fit the typical experimental results, are shown in Figs. 5(a) and 5(b). Figures 5(a) and 5(b) show that our model and the experimental results are strongly correlated. Our model fits the experimental data from all liver samples well. The coefficient of determination R^2 between our model and the experimental data from the time series of displacement in all samples at all stresses exceeded 99%. Each data set was fitted with a pair (x_c, α), and then the results were averaged. Tables I and II list the model accuracy evaluation and

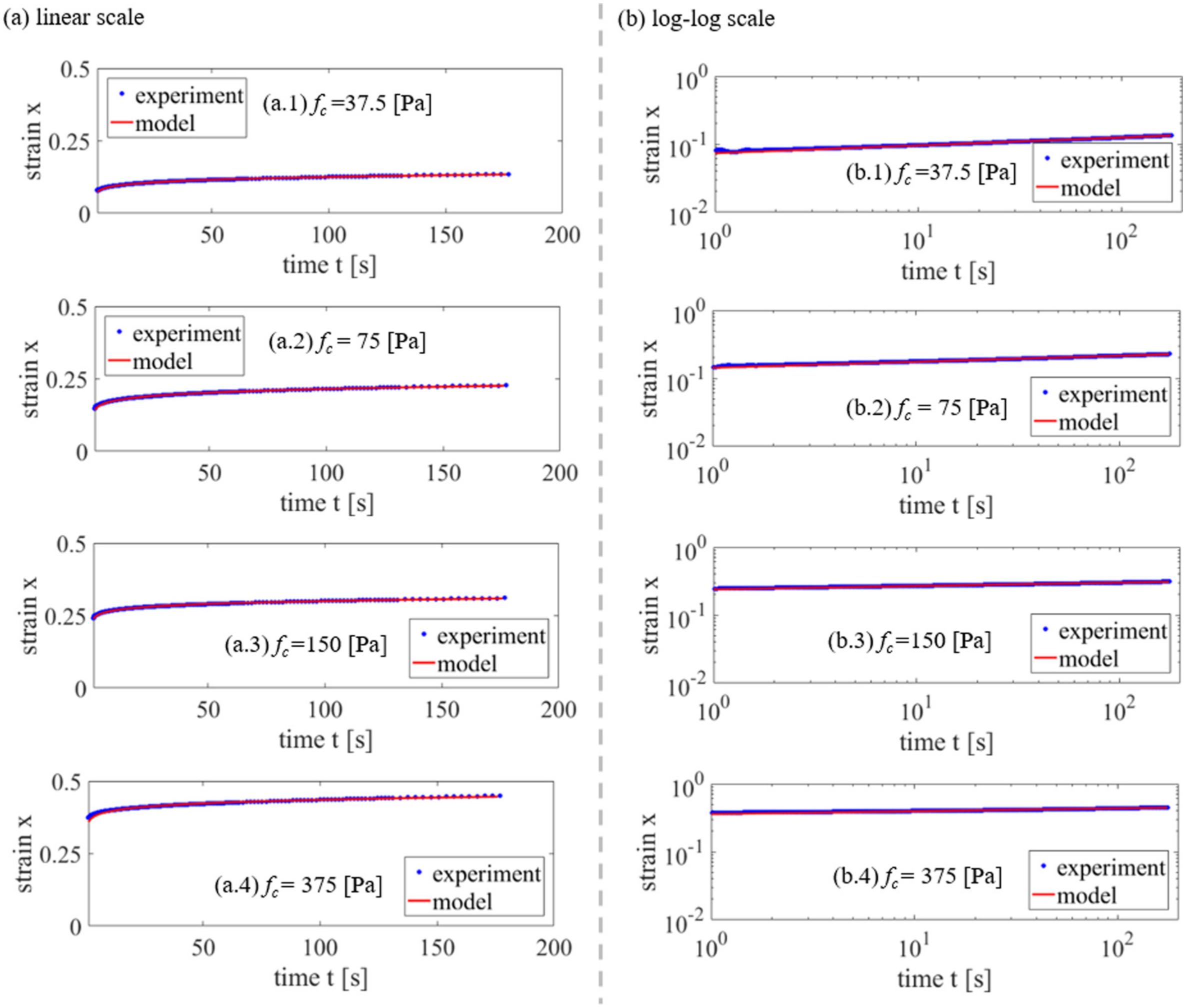

FIG. 5. Creep test (step response). (a) A typical example of experimental results of a creep test, the creep response obtained by assuming the input step stress f_c. (b) A log-log diagram of the same data described in (a). The plots in (a) and (b) are the experimental results. The strain of the sample increased over a time interval of 180 s. We found that the time series data of the creep response exhibited a power law form over two decades. The lines are the time series data of our model. Our model equation represents the trend observed in the experimental results. This figure shows that our model and the experimental results are highly correlated.

fundamental statistics of the model parameters. For example, the average data of (x_c, α) are shown in Tables I and II.

D. Nonlinearity measurement

The nonlinear properties of samples were investigated based on a series of creep tests under several applied stresses f_c. Specifically, we examined the relationship between the constant applied stress f_c and the strain coefficient x_c in a series of creep tests using several stresses. Typical experimental results for nonlinearity measurement of the sample are shown in Figs. 6(a) and 6(b). Figure 6(b) shows a semilog diagram of the same data described in Fig. 6(a). Figure 6(a) shows that the relationship between x_c and f_c exhibits linear characteristics under low strain conditions. The stress nonlinearly increased under high strain conditions. Figure 6(b) shows that the stress increase during high displacement is linear in the semilog scale; stress increases exponentially in the linear scale space. We found that the linear straight line and nonlinear curves connected smoothly, with the exponential curve being tangent to the straight line in the linear region. We modeled the nonlinear properties of the soft biological tissue based on these results and considerations, as shown in Eqs. (19a) and (19b):

$$G x_c = f_c \quad \{x_c < x_b\}, \tag{19a}$$

$$G x_b e^{\frac{x_c - x_b}{x_b}} = f_c \quad \{x_c > x_b\}. \tag{19b}$$

The other form of Eq. (19b) is as follows:

$$G_i e^{G_n x_c} = f_c \quad \{x > 1/G_n\}. \tag{20}$$

Here, x_c is strain and f_c is stress. G is a proportionality factor (referred to as linear viscoelastic stiffness or linear stiffness herein), x_b is the boundary strain between the linear and nonlinear range (called simply boundary strain), G_n is a proportionality factor in log space (called nonlinear viscoelastic stiffness or nonlinear stiffness), and G_i is the dependent parameter.

Each parameter should fulfill the following relationship due to the exponential curve (19b) being tangent to the straight line

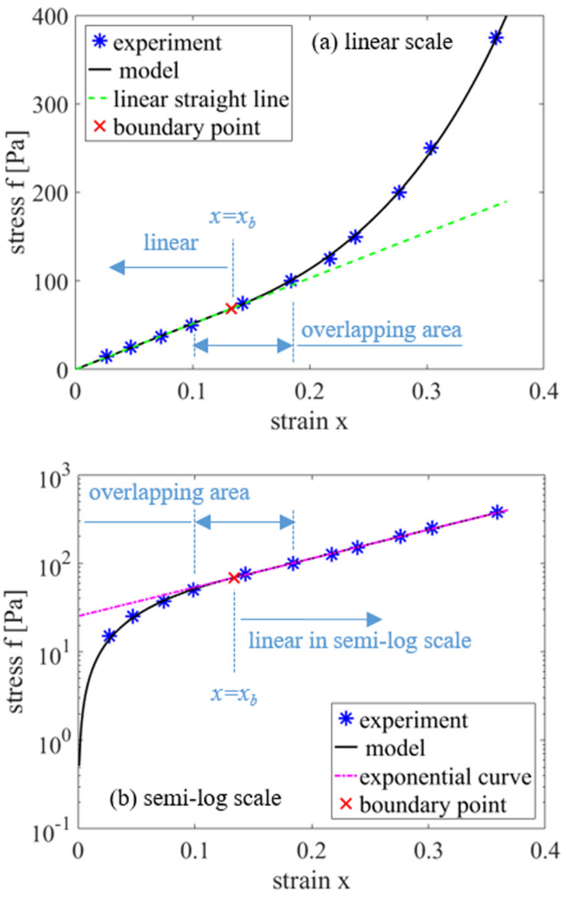

FIG. 6. Nonlinearity measurement. Typical experimental results when $t_r = 1$ are shown in (a) linear scale and (b) semilog scale. (a) Shows that the relationship between strain x_c and stress f_c exhibits linear characteristics under low strain conditions. (b) Shows that the stress increase during high displacement is linear in the semilog scale; stress increases exponentially in the linear scale space. We found that the linear straight line and nonlinear curves connected smoothly, with the exponential curve tangent to the straight line in the linear region. The stress-strain relationship of our model, which fits the typical experimental results, is shown by the line. Our model and the experimental results are highly correlated. There is an overlapping area, where the results exhibit both linear dependence and exponential law dependence. Linearity holds to a certain degree above the boundary strain x_b, and exponential law dependence holds to a certain degree below the boundary strain x_b.

(19a) (details of this relationship are shown in Appendix E):

$$G_n = \frac{1}{x_b}, \quad G_i = \frac{G x_b}{e}. \tag{21}$$

The following equations (22a) and (22b) are derived from the natural logarithm of both sides in (19b) and (20), respectively:

$$\frac{x_c}{x_b} = \ln\left(\frac{e}{G x_b} f\right) \quad \{x_c > x_b\}, \tag{22a}$$

$$G_n x_c = \ln\left(\frac{G_n e}{G} f\right) \quad \left\{x_c > \frac{1}{G_n}\right\}. \tag{22b}$$

The parameters (G, G_n, G_i, and x_b) of Eqs. (19a) and (22b) were identified by fitting the experimental results for each sample. We used the EKF algorithm to identify the parameters of Eqs. (19a) and (22b) (see Appendix G for details), as they are nonlinear simultaneous equations. The stress-strain relationship of our model, which fits the typical experimental results, is shown in Fig. 6, and shows that our model and the experimental results are strongly correlated. Our model also fits the experimental data from all liver samples well. The coefficient of determination R^2 between our model and the experimental data in all samples was approximately 95%. Each data set was fitted with a pair (G, G_n), and then the results were averaged. Tables I and II list the model accuracy evaluation and fundamental statistics of model parameters. For example, the average data of (G, G_n) are shown in Tables I and II.

Thus, we derived the nonlinear equations for our model shown in (1a) and (1b). This section derived the static equation of the FDEN model (in the case of $\alpha = 0$). We assume here that Eqs. (19a) and (19b) can hold true in a more general situation for strain x and stress f in the absence of creep tests. Moreover, we assume that the nonlinear relationship between x_c and f_c still holds at arbitrary α more generally because coefficients f_c and x_c in Eq. (16) are defined as time-independent parameters, and these parameters are valid for arbitrary α in Eq. (16).

IV. DISCUSSION

The main contribution of this article is the proposal of a fractional dynamics and exponential nonlinearity (FDEN) model to identify the rheological properties of soft biological tissue. We found from experimental results that biological tissues have specific properties: (i) power law increase in the storage elastic modulus G' and the loss elastic modulus G'' of the same slope ($G', G'' \propto \omega^{\alpha}$); (ii) power law compliance (gain) J and constant phase delay ϕ in the frequency domain ($J \propto \omega^{-\alpha}$, $\phi = -\frac{\pi}{2}\ \alpha$) over two decades; (iii) power law dependence between time and strain relationships ($x \propto t^{\alpha}$) over two decades; and (iv) linear dependence in the low strain range ($f \propto x$) and exponential law dependence ($\ln f \propto x$) in the high strain range between stress-strain relationships. The FDEN model uses only three dependent parameters, such as α, G, and x_b (or G_n), and represents the specific properties of soft biological tissues. The advantage of our model is that it strongly correlates with various experimental data, as shown in Sec. III. In addition, the small number of parameters used is valuable because it is suitable for parameter identification and inverse analysis. For example, the parameter identification methods in this article are basic, with only the LSM and EKF being used. Lastly, the meaning of each parameter is intuitively understood (e.g., α: ratio of viscoelasticity, G: linear stiffness, G_n: nonlinear stiffness, x_b: boundary strain between the linear and nonlinear range) and it is possible to compare the values with those of other tissues. The details are discussed in the following sections.

A. Viscoelastic model using fractional calculus

We found from experimental results that soft biological tissues have specific viscoelastic properties, as described above in (i)–(iv). Single terms in the fractional dynamics model (1a) represent the specific properties of soft biological tissues.

Fractional calculus is an approach to mathematically describe natural phenomena that are related to viscoelastic behavior [41]. It is a branch of mathematical analysis concerned with taking real or complex number powers of differential operators. Fractional dynamics is a field of study in physics and mechanics concerned with investigating the behavior of objects and systems that are characterized by power law nonlocality, power law long-term memory, or fractal-type properties by using integration and differentiation of noninteger orders, i.e., by fractional calculus methods [42]. Fractional dynamics models are powerful tools in describing the dynamic behavior of various materials. The advantages of fractional dynamics models are their ability to describe real dynamic behavior and the fact they are simple enough for engineering calculations [43]. The equations for viscoelastic models are generally based on stress-strain analyses and are traditionally represented with derivatives of integer order (ordinary differential equations). In other words, traditional methods to fit the viscoelastic response include several spring and dashpot elements. Recently, fractional dynamics models proved to be efficient in describing rheological materials such as rubber and tissues, reducing the number of parameters and showing a power law response [44].

Over the last few years, fractional calculus has become an important tool in the analysis of viscoelastic materials composed of synthetic polymers [45]. For example, Caputo *et al.* [46–48] found good agreement with experimental results when using a fractional calculation for the description of viscoelastic materials and established the connection between the fractional calculation and the theory of linear viscoelasticity [49]. Several authors [50,51] have also suggested the use of differential or integral equations of fractional order to describe viscoelastic behavior that is intermediate between purely elastic and purely viscous [52].

Although fractional calculus is widely applied in describing the solid-liquid duality of synthetic polymers, it had until recently attracted limited attention in the field of biological materials, biomechanics, and bioviscoelasticity [53]. Suki *et al.* [54] found the pressure and volume response of a whole lung to be characterized by fractional calculus. Fractional calculus is also useful in biology-related fields because many tissuelike materials (polymers, gels, emulsions, composites, and suspensions) exhibit power law responses to applied stress or strain [55]. Yuan *et al.* [56] studied lung tissue and found its fractional order of evolution, while Chen *et al.* [57] applied the same model to agarose gels used for culturing tissues, particularly cartilage. An example of the power law behavior of elastic tissue was observed recently for viscoelastic measurements of blood vessels, where the analysis of these data was most conveniently performed using fractional order viscoelastic models [55]. Recent studies reveal that fractional calculus can be used to model smaller components such as cells [57–59]. The framework of fractional calculus has also been used in research on magnetic resonance elastography [53,60]. As above, fractional dynamics is gaining popularity in the field of viscoelasticity, with data and models already reported for the liver [32–35], breast tissues [37], lung [54,61], vessels [44], muscle [38,39], brain [62], tendons [63], muscle cells [57], blood cells [58], and living cells [59]. In short, research on fractional calculus has been applied widely to many fields, including biological materials.

The parameter α in fractional equation (1a) is the derivative order and is commonly taken to range between 0 and 1. If α is 0, Eq. (1a) describes the behavior of a spring where G specifies the spring's stiffness. If α is 1, Eq. (1a) defines a dashpot, in which G defines the viscosity. Thus, the fractional equation (1a) interpolates between the material behavior of a spring and that of a dashpot [49]. The rheological element that refers to Eq. (1a) was therefore introduced by Koeller and termed a "springpot" [55,64]. As such, the derivative order α represents the index of viscosity of the system in the fractional dynamics model. A viscoelastic material is more governed by elastic properties than by the viscous properties when the derivative order α is close to 0, and vice versa when the derivative order α is close to 1.

The value of the derivative order α was approximately 0.125 $(=\frac{1}{8})$ from the experimental results presented in this article, indicating that the characteristics of soft biological tissue (liver) are intermediate between those of elastic and viscous bodies and that this tissue is relatively close to an elastic material.

B. Fractional calculus for the dynamic viscoelastic and creep tests

In this article, the viscoelastic properties of soft biological tissues (liver) have been examined. The simple empirical equations describing strain creep [Eqs. (16) and (18)] have been put in a concise mathematical framework. We have chosen to describe viscoelasticity in terms of a fractional calculation as in Eq. (1a). Certain important advantages of fractional calculus must be emphasized [44,54]: (i) fractional dynamics models accurately describe complex models with fewer parameters, (ii) they improve curve fitting, principally with power law responses, and (iii) they allow for a physical justification of fractal structure of soft biological tissue, as described in the Sec. IV C.

1. Dynamic viscoelastic test

Measurements of mechanical complex impedance G^* in dynamic viscoelastic tests over a wide range of forcing frequencies (10^{-1}–10^{1} rad/s) in tissue samples revealed that the frequency dependence of rheological behavior represents a weak power law relationship over a wide range of frequencies ($G', G'' \propto \omega^{\alpha}$). For example, Fabry [65] reported that a weak power law relationship held over a range of frequencies (10^{-2}–10^{3} Hz) in muscle cells. The storage modulus G' increases with increasing frequency according to a weak power law ($G' \propto \omega^{\alpha}$) with a power law exponent of approximately 0.125 ($\alpha = 0.125 = \frac{1}{8}$). The loss modulus G'' also follows the power law ($G'' \propto \omega^{\alpha}$) with a power law exponent of approximately 0.125 ($\alpha = 0.125 = \frac{1}{8}$). Fractional calculus provides a natural framework for describing such weak power law relationships [63].

In contrast, mechanical models using ordinary differential equations have long been used, and their qualitative behavior is not representative of the actual behavior of materials. The characteristics of the frequency dependencies could be similar;

however, the slopes of the experimental results do not fit those of the theoretical curves [43]. The shortcomings of ordinary differential models can be recognized by comparing the frequency curves exhibited by a material with those predicted by the models. The weak power law behavior cannot be accounted for by standard viscoelastic models characterized by ordinary differential equations [63]: (i) storage modulus G' should remain constant ($G' = \text{const}$) at low frequencies, which would indicate elastic behavior in ordinary differential equations and (ii) loss storage modulus G'' increases and approaches a power law exponent of 1 ($G'' \propto \omega$) at high frequencies, indicating viscous behavior in ordinary differential equations.

2. *Creep test*

Recent studies also indicated that the time domain data of tissues are well represented by a simple empirical equation involving a power law in time [$x(t) \propto t^{\alpha}$]. Some studies also reported that creep responses represent power law stress to a step input in the time domain. Fung [1] demonstrated in his theory that a distribution of time constants proportional to power of time over a finite range of time constants is appropriate for many tissues [54]. Djordjevic and co-workers [63] reported that a parallel combination of a fractional calculus (springpot) and a dashpot properly predict the measured values for a rheological model of cultured smooth muscle cells [55]. As above, fractional calculus provides a natural framework for describing such power laws in the time domain [63].

In contrast, mechanical models using ordinary differential equations lack consistency between their qualitative behavior and the real behavior of material curves. Although the characteristics of time dependencies could be similar, the slopes of experimental results do not fit those of the theoretical curves. The shortcomings of ordinary differential models can be recognized by comparing the time domain curves observed for a material with those predicted by the models [43]. The power law behavior cannot be accounted for by standard viscoelastic models characterized using ordinary differential equations, such that (i) strain should remain constant at sufficient elapsed times [$x(t) \rightarrow \text{const}$ at $t \rightarrow \infty$], which would indicate elastic behavior in ordinary differential equations; and (ii) exponential increases in transient state [$x(t) = x_o(1 - e^{t/T})$], which would indicate viscous behavior in ordinary differential equations.

C. Fractal structure and the fractional ladder model

Theoretical aspects of the fractional calculus of soft biological tissue are partially explained with fractal geometry [66] and holonic systems [67] in nature. Currently, fractal geometry and fractional calculus are applied to phenomenological theories for complex systems [41]. Soft biological tissues also have fractal structures, such as in Fig. 7. A fractal is a natural phenomenon or a mathematical set that exhibits a repeating pattern displayed at every scale. For example, Schiessel and Blumen [45], Schiessel *et al.* [68], and Heymans and Bauwens [52] have demonstrated that fractional equations, such as (1a), can be realized physically through the fractal structure of hierarchical arrangements of springs and dashpots like ladders [69]. Figure 7(a) displays an infinite number of thin elastic membranes and viscous compartments. Figure 7(b) is a magnified region of Fig. 7(a), and Fig. 7(c) is a magnified region of Fig. 7(b), showing the self-similar layered structure. By allowing the number of structural components to extend indefinitely, the self-similarity of biological media is revealed. This topology is also depicted in Fig. 7, where the alternating elastic and viscous components are visualized as a self-similar hexagonal packing of spheres within spheres [70]. A related work [70] describes the details of the following layered fractal models of soft biological tissues based on the schema shown in Figs. 7 and 8. In order to capture these fractal components with the elastic membranes and viscous saline of biological tissue, a fractal ladder of springs and dashpots in Fig. 9 is introduced [70]. A paper [70] described the properties of the model shown in Fig. 9(a), which presents the fractional derivative term with derivative order $\frac{1}{2}$. Similar fractal tree networks were considered [70] to model other orders of fractional calculus.

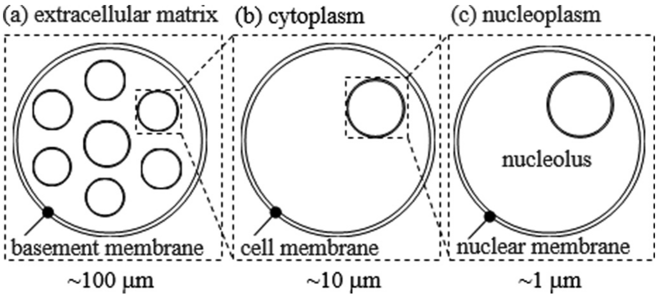

FIG. 7. Fractal structure of soft biological tissues [70]. A repeating pattern with thin elastic membranes and viscous components is displayed at every scale. Panel (a) displays an infinite number of thin elastic membranes and viscous compartments. Panel (b) is a magnified view of panel (a), and panel (c) is a magnified view of panel (b), thus showing the self-similar layered structure. By allowing the number of structural components to extend indefinitely, the self-similarity of biological media is revealed.

The fractal ladder model is defined with self-recursive properties, which result from the fractal structure, to explain the linear fractional model. In other words, the fractal ladder model is constructed with the same fractal ladder model as in Fig. 8. For example, the fractional order term with ($\alpha = \frac{1}{2}$) is derived using spring term ($\alpha = 0$) and viscous term ($\alpha = 1$) from the self-similar properties. The properties $P(s)$ of overall part (a) are the same as those for the dotted area (b) in Fig. 8; in other words, the properties of part (b) are also $P(s)$. Then, the following equation holds from the self-similar properties:

$$P(s) = \frac{1}{\frac{1}{k} + \frac{1}{P(s)+cs}}. \tag{23}$$

Here, $P(s)$ is the Laplace function of overall properties. The following equation (24) is derived from the expansion of (23):

$$P(s)^2 + csP(s) - kcs = 0. \tag{24}$$

The following equation (25) is obtained by solving Eq. (24):

$$\begin{aligned} P(s) &= \frac{-cs + \sqrt{(cs)^2 + 4kcs}}{2} \\ &= k\frac{-\frac{c}{k}s + \sqrt{\frac{c}{k}s\left(\frac{c}{k}s + 4\right)}}{2}. \end{aligned} \tag{25}$$

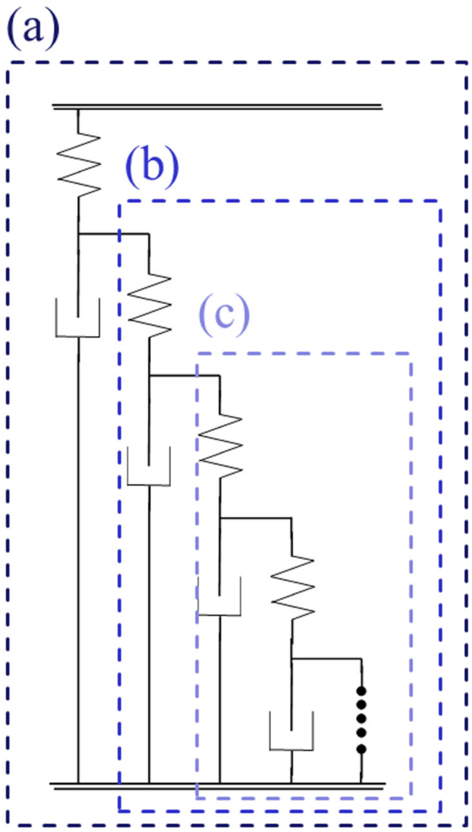

FIG. 8. The fractal ladder model. The model is defined with self-recursive properties, which result from the fractal structure, to explain the linear fractional model. The fractal ladder model is constructed with the same fractal ladder model. This figure explains that the fractional order term with ($\alpha = \frac{1}{2}$) is derived using spring term ($\alpha = 0$) and viscous term ($\alpha = 1$) from the self-similar properties. The properties $P(s)$ of overall part (a) are the same as those for the dotted area (b) and also (c); in other words, the properties of parts (b) and (c) are also $P(s)$.

For $(cs)/k \ll 1$, the binomial approximation is applied, yielding the law frequency approximation

$$P(s) = \sqrt{kc}\,s^{1/2}. \tag{26}$$

Thus, $P(s)$ is a fractional order term with $\alpha = \frac{1}{2}$. Generally, a fractional order term with $\alpha = n/2m\{(0 < \alpha < \frac{1}{2}) \wedge (n,m \in N)\}$ is generated in the same manner through the iterated calculation of the fractal ladder model using the fractional term. Here, the fractal ladder model, which was constructed using the fractional derivative term with α_k and α_c, is considered. The properties of overall part $P'(s)$ are the same as those for the dotted area. Then,

$$P'(s) = \frac{1}{\frac{1}{p_k s^{\alpha_k}} + \frac{1}{P'(s) + p_c s^{\alpha_c}}}. \tag{27}$$

The following equation is obtained by solving the above equation:

$$P'(s)^2 + p_c s^{\alpha_c} P'(s) - p_k p_c s^{\alpha_k + \alpha_c} = 0. \tag{28}$$

The following equation is obtained by solving the above equation:

$$\begin{aligned} P'(s) &= \frac{-p_c s^{\alpha_c} + \sqrt{(p_c s^{\alpha_c})^2 + 4 p_k p_c s^{\alpha_k + \alpha_c}}}{2} \\ &= p_k \frac{-\frac{p_c}{p_k} s^{\alpha_c} + \sqrt{\frac{p_c}{p_k} s^{\alpha_c}\left(\frac{p_c}{p_k} s^{\alpha_c} + 4 s^{\alpha_k}\right)}}{2}. \end{aligned} \tag{29}$$

For $p_c s^{\alpha_c}/p_k \ll 1$, the binomial approximation is applied, yielding the law frequency approximation

$$P'(s) = \sqrt{p_k p_c}\, s^{(\alpha_k + \alpha_c)/2}. \tag{30}$$

The $\frac{1}{4}$- and $\frac{1}{8}$-order fractional terms (springpots) are derived from the above calculation using $(\alpha_k, \alpha_c) = (0, \frac{1}{2})$ and $(0, \frac{1}{4})$, respectively.

These recursive ladder expansions provide various derivative order parameters. Specifically, the ladder model can also be considered as a fundamental mechanical component of the fractional derivative term, allowing more complex fractal networks, or recursive ladders, to be constructed.

For instance, consider a recursive ladder model constructed by replacing the viscous damper in Fig. 9(a) with a fractal ladder, producing the arrangement shown in Fig. 9(b) with derivative order $\alpha = \frac{1}{4}$. Similarly, a recursive ladder may be constructed by replacing the springs in Fig. 9(b) with a fractal ladder, producing the arrangement shown in Fig. 9(c) with derivative order $\alpha = \frac{1}{8}$.

Here, we introduced the fractal structure of soft biological tissue and the relationship between fractal structure and fractional calculus geometrically. The calculations in this section (23)–(30) also reveal that soft biological tissue has holonic properties, where a holon is something that is simultaneously a whole and a part [67]. For example, the overall finite ladder model shown in Fig. 8(a) functions first as a whole, while the finite ladder model shown in Fig. 8(b) functions first as a part. Thus, the same finite ladder model acts as a holon: both a whole and a part.

D. Main contribution

From the perspective of fractional calculus, the main contribution of this study is to propose integration with fractional calculus and nonlinear equations, in other words, utilizing the nonlinearity of fractional calculus, a prefactor that switches smoothly from linear line to exponential curve, to describe soft biological tissue. The history of using fractional dynamics in the study of viscoelastic materials is long standing; however, the nonlinearity of the fractional term for soft biological tissue has not yet been considered in related studies.

The measured exponent α, close to $\frac{1}{8}$, suggests that the liver tissue is mechanically equivalent to a cubed fractal structure (fractal of a fractal of a fractal) whose basic elements are elastic and viscous elements (refer to Fig. 9). The structure of soft biological tissue is generally and reasonably considered as a simple fractal structure with elastic membrane and viscous fluid, as shown in Fig. 7. The experimental results with cubed fractal structure raise the issue of the actual structure of soft

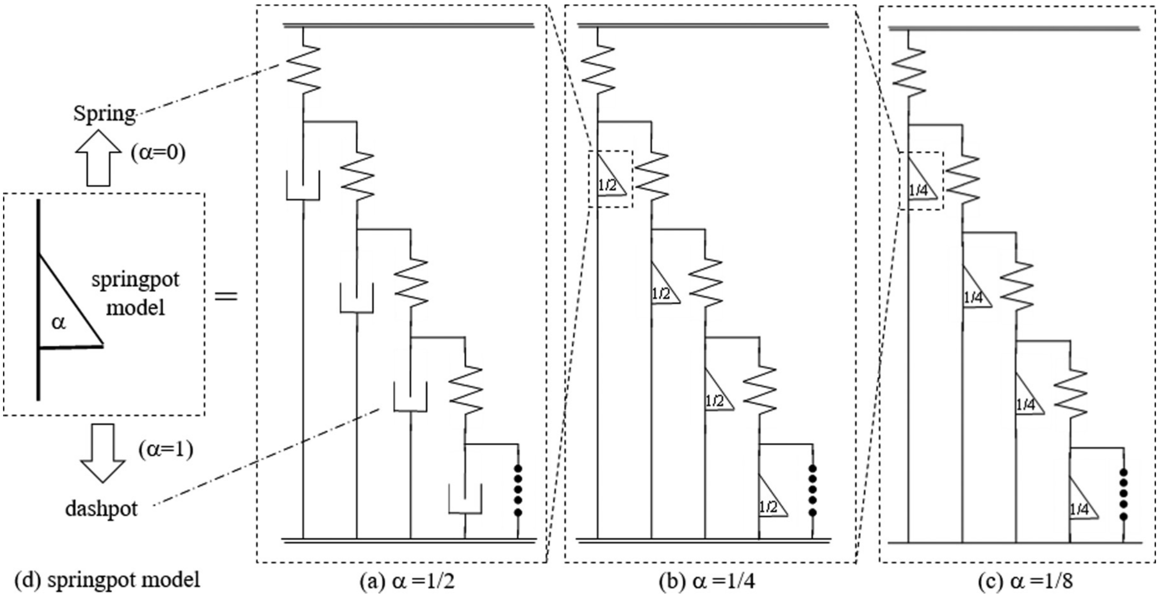

(d) springpot model (a) α =1/2 (b) α =1/4 (c) α =1/8

FIG. 9. Fractal ladder of springs and dashpots in order to capture these fractal components with the elastic membranes and viscous saline of biological tissue. Fractal tree networks were considered to model fractional calculus [orders α of $\frac{1}{2}$, $\frac{1}{4}$, and $\frac{1}{8}$ are described in (a), (b), and (c), respectively]. These recursive ladder expansions provide various derivative order parameters of a springpot model (d). Specifically, the ladder model can also be considered as a fundamental mechanical component of the fractional derivative term, allowing more complicated fractal networks, or recursive ladders, to be constructed. The parameter α (derivative order and also power law exponent) was approximately $\frac{1}{8}$ $(= 0.125)$ according to the experimental results of the dynamic viscoelastic tests in Figs. 3 and 4. This result suggests that liver tissue has a complex fractal structure such as in (c), where the liver tissue is mechanically equivalent to a cubed fractal structure (fractal of a fractal of a fractal) whose basic elements are elastic and viscous elements.

biological tissue; how it could be related to a cubed fractal structure remains obscure.

The fractional model with a single term is most suitable for the identification of biorheological properties, while many previous studies also have proposed serial and/or parallel arrangements of ordinary order models and fractional order models (such as a fractional generalized Voigt model with a fractional term). The single fractional derivative term has the strong advantage of high model accuracy, although the frequency range was relatively low in this study, and the power law relationship is suitable for parameter identification, as described in Secs. IV F, IV G, and IV H.

E. Exponential nonlinearity

Figure 6 and Eq. (19b) show that stress on soft biological tissue increases exponentially with strain. Exponential trends are generally known in fields such as economics and in natural evolutionary processes. For example, value grows exponentially with time, technology has advanced at an exponential rate [71] (exponential growth of computing power is known as Moore's law), market price in inflation shows exponential growth [72], and population growth (such as Malthusian Theory of Population) is exponential. The experimental results of stress and exponential models imply that the behaviors in the stress-strain relationship may have similar mathematical and physical structures, although the variable is not time but strain. In this theory, the exponential growth evolves due to a linear positive feedback mechanism, such as Eq. (31b); an upward change in stress induces further increases in stress rather than just incremental additions:

$$\begin{cases} \dfrac{d^\alpha \varphi}{dt^\alpha} = f \\ \dfrac{\partial^2 \varphi}{\partial x^2} = 0 \end{cases} \quad \{-x_b < x < x_b\}, \tag{31a}$$

$$\begin{cases} \dfrac{d^\alpha \varphi}{dt^\alpha} = f \\ \dfrac{\partial^2 \varphi}{\partial x^2} = \left(\dfrac{1}{x_b}\right)^2 \varphi \end{cases} \quad \{x > x_b\} \vee \{x < -x_b\}, \tag{31b}$$

where φ is the intermediate variable between the upper and lower equations. We introduce a second-order partial differential equation here because of the negative and positive symmetry properties of the stress-strain relationship, as shown in Fig. 10 and Eq. (32). The solution for the second-order partial differential equation is as follows:

$$-Gx_b e^{-\frac{x+x_b}{x_b}} = f \quad \{x < -x_b\}, \tag{32a}$$

$$Gx = f \quad \{-x_b < x < x_b\}, \tag{32b}$$

$$Gx_b e^{\frac{x-x_b}{x_b}} = f \quad \{x > x_b\}. \tag{32c}$$

Here, the solution for the first-order partial differential equation only represents positive or negative exponential stress changes.

The smoothness of a fundamental mathematical function largely affects the robustness of identification, inverse analysis, structure analysis in computer simulations, and optimization

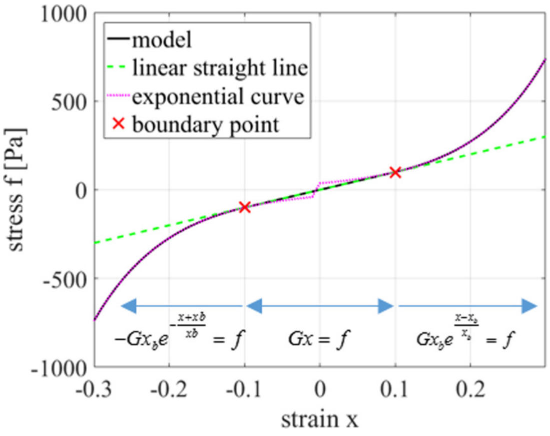

FIG. 10. Negative and positive symmetry property of stress-strain relationship to introduce the second-order partial differential equation (in the case of $G = 1000$ and $x_b = 0.1$). The solution of the first-order partial differential equation only represents positive or negative exponential stress changes. The solution of the second-order partial differential equation represents positive and negative exponential stress changes, such as those shown in this figure.

using structure analysis. In particular, the smoothness at a point where the mathematical function changes (specifically, $x = x_b, -x_b$) is important. Differentiability class is generally used in the classification of functions according to smoothness, more specifically, the properties of their derivatives. The differentiability class of our nonlinear model, between equations such as (19a) and (19b), (32a) and (32b), and (32b) and (32c), is $C1$ at $x = x_b, -x_b$; this means curves are continuous and differentiable at $x = x_b, -x_b$. In other words, curves are joined and their first derivatives are continuous at $x = x_b, -x_b$. Thus, the smoothness of the function in our nonlinear model is maintained (the differentiability class is $C1$) when compared with linear models. The mathematical process to explain the connectivity is shown in Appendix E. These smooth characteristics are an advantage of our model because the robustness of calculations in the boundary between linear and nonlinear characteristics is high.

We can estimate the origin of strain from data in the nonlinear range due to the constraint condition of parameters described in Eq. (21) because of the properties of an exponential function. The subtangent, which is a geometric term meaning certain line segments defined using the line tangent to a curve at a given point and the coordinate axes, is constant in an exponential function. Moreover, the value of the subtangent is x_b in our model. The subtangent can be estimated using the tangent (G_n) of the semilog graph of the stress-strain relationship: $x_b = \frac{1}{G_n}$ (refer to Fig. 10). This is an important characteristic because the zero strain point of soft biological tissue is generally difficult to define for the following reasons: (i) the zero strain point cannot be defined from linear data; (ii) the deformation of soft biological tissue is relatively large and is markedly affected by gravitational force; and (iii) the viscoelasticity of soft biological tissue makes measuring the zero strain point difficult. We can estimate the zero point from the value of x_b via an exponential function with G_n in the nonlinear range.

F. Time and frequency scale invariance

One attribute of power laws is their scale invariance. Scaling the argument by a constant factor causes only a proportionate scaling of the function itself. Scaling by a constant simply multiplies the original power law relationship by the constant (parameter α in this article). Thus, it follows that all power laws with a particular scaling exponent are equivalent up to constant factors, as each is simply a rescaled version of the others. There is no internal time scale that could typify the dynamics, and no time characteristics are evident.

Time scale invariance during creep tests can be described based on the above discussion, and creep response is not tied to any time scale; thus, it may be regarded as being scale free. More specifically, as explained in this article, obtaining numerous time series data from creep tests is not necessary due to invariance in the time scale property. Only two data points (t_1,x_1) and (t_2,x_2) at any time point are sufficient to identify the parameter of Eq. (18): $\alpha = \frac{\log(x_2/x_1)}{\log(t_2/t_1)}$, $x_c = \frac{x_1}{(t_1/t_r)^\alpha}$ and $G = \frac{f_c}{x_c\Gamma(1+\alpha)}$. Naturally, this is only a theory pertaining to identical conditions, and many data points are preferable to enhance the robustness of measurements.

Frequency scale invariance during dynamic viscoelastic tests can be described in the same manner. There are no internal frequency scales that could typify the dynamics, and no characteristic frequency was evident. Mechanical impedance responses are not tied to any frequency scale; thus, they may be regarded as being scale free. More specifically, obtaining numerous frequency series data from dynamic viscoelastic tests is not necessary due to invariance in frequency scales. Only two data points (ω_1,J_1) and (ω_2,J_2) at any frequency point are sufficient to robustly identify the parameter of Eq. (14): $\alpha = -\frac{\log(J_2/J_1)}{\log(\omega_2/\omega_1)}$ and $J_o = 1/G = \frac{J_1}{(\omega_1/\omega_r)^{-\alpha}}$. As for time scale invariance, this is only a theory pertaining to identical conditions, and many data points are preferable to enhance the robustness of measurements.

G. Strain scale invariance

Strain scale invariance, while nonlinearity is not a power law, also holds at the linear area and nonlinear scale. The relationship between stress and strain in the linear range exhibits strain scale invariance because of linearity. The relationship between the logarithms of stress and strain in the nonlinear range also exhibits strain scale invariance because of the exponential law dependence. This scale invariance produces a strong relationship for identifying parameters. Theoretically speaking, a two-point data set containing only (x_{c1},f_{c1}) and (x_{c2},f_{c2}) in the linear range is sufficient to identify linear stiffness G (slope of stress and strain in the linear space): $G = \frac{f_{c2}-f_{c1}}{x_{c2}-x_{c1}}$. Moreover, zero point $(x_{c1},f_{c1}) = (0,0)$ can be included to calculate this process: $G = \frac{f_{c2}}{x_{c2}}$. In addition, a two-point data set in the nonlinear range is sufficient to identify nonlinear stiffness G_n (slope of stress and strain in the semilog space): $G_n = \frac{\ln(f_{c2}/f_{c1})}{x_{c2}-x_{c1}}$. Of course, the aforementioned numbers for this data set are theoretical for identical situations, and many data points are preferable to enhance measurement robustness.

In addition, strict classifications between the linear and nonlinear ranges should not be necessary because of the smooth connectivity between the linear and nonlinear properties of soft biological tissues (Fig. 6). There is an overlapping area where both linearity and exponential law dependence hold. Linearity holds to a certain degree beyond the boundary strain x_b. Furthermore, the exponential law dependence holds to a certain degree before the boundary strain x_b. In other words, the data set in the overlapped area includes information from both the linear and nonlinear ranges. These properties, which are common to soft biological tissues and the FDEN model, are useful for identifying parameters, and it is possible to identify both linear and nonlinear stiffness using only data sets derived from the overlapping area: both $G = \frac{f_{c2}-f_{c1}}{x_{c2}-x_{c1}}$ and $G_n = \frac{\ln(f_{c2}/f_{c1})}{x_{c2}-x_{c1}}$. However, further research is required to confirm this hypothesis.

H. Identification algorithm

According to the simple model equation, its power law properties, and its exponential law dependence, parameter identification in the FDEN model is simpler when compared to other reported models. The small number of parameters in the FDEN model contributes to a simple algorithm and parameter identification. These characteristics may also be effective in inverse analysis of computer structural simulations of tissue and organ deformation. For example, the parameter identification methods in this article are basic, with only LSM and EKF being used. The parameters of the model in the creep test can be identified using LSM. EKF was used to identify the parameter of the dynamic viscoelastic tests, mechanical impedance, because Eqs. (11a) and (11b) are nonlinear simultaneous equations. EKF was also used to identify the parameter of nonlinear models between the stress-strain relationship because Eqs. (19a) and (22b) are nonlinear simultaneous equations.

The parameters of the model in the Bode diagram were identified via parameter identification of mechanical impedance in this article. It should be noted that LSM is sufficient to identify the values of α and G in (14) using the data set of compliance (gain) J . The correlation between model (15) and the experimental data of the phase ϕ should be carefully checked in this case, as phase data can affect identification of the parameters.

I. Parameter variation

Tables I and II list the model accuracy evaluation and fundamental statistics of model parameters. Statistical analysis of the samples used in this study revealed that the maximum values of α, G, and G_n were approximately 1, 4, and 3 times the minimum values, respectively. These results indicate that the linear stiffness G and the nonlinear stiffness G_n (also, x_b as an independent parameter) have a large degree of variation when compared with the ratio of viscoelasticity α. The one limitation of this study is that the number of samples was insufficient to statistically analyze the variations in each parameter. We plan to study other tissue types in order to compare and discriminate between tissues using these static and variable parameters (e.g., [37]).

J. Limitations

The main limitation of this study is that we only measured and evaluated liver samples. Similar evaluations must be performed with other tissues in order to clarify the universality of the FDEN model. This will allow us to clarify the applicability of our model to various tissue types. We believe that the FDEN model can represent other biological tissues consisting of a single tissue type, excluding nonsoft tissues and tissue exhibiting plasticity. Our previous nonlinear viscoelastic model with four parameters [32–35] has already been partially evaluated using breast tissues (fibroglandular tissue, fat, muscle) [36,37]. We plan to evaluate the FDEN model using other tissues in future studies.

The theoretical limitation of this article is in the derivation of the nonlinear equation: we assume power law dependence holds in the single creep test. We will research theoretical discussion of this point in future work (for example, the relationship with yield strain in [73]) because this article only covers the feasibility of power law approximation in the creep test. The coefficient of determination R^2 between our model and the experimental data from the time series of displacement in all samples at all stresses exceeded 99%, as shown in Table I. We also describe the feasibility of the approximation mathematically in Appendix D.

Another limitation of this study is the lack of stress relaxation and indentation tests. These are basic tests to evaluate viscoelastic properties and stress-strain nonlinearity, respectively. Parameter identification in the FDEN model using these tests is described in Appendixes H and I. Stress relaxation analysis using fractional viscoelasticity was introduced in related studies [50,51], as well as in our work on human stretch applications [39]. Moreover, indentation (in the case of needle insertion and palpation for medical robotics) using the nonlinear model has been introduced in related studies [32–37].

V. CONCLUSION

We proposed a simple empirical model using fractional dynamics and exponential nonlinearity (FDEN) to identify the rheological properties of soft biological tissue. The model is derived from detailed material measurements using samples isolated from porcine liver. We conducted dynamic viscoelastic tests and creep tests on liver samples using a rheometer. The experimental results indicated that biological tissue has specific properties, such as (i) power law increase in the storage elastic modulus and the loss elastic modulus with the same slope; (ii) power law compliance (gain) decrease and constant phase delay in the frequency domain over two decades; (iii) power law dependence between time and strain relationships under constant force; and (iv) linear and exponential dependence that switches smoothly between stress-strain relationships. Our simple FDEN model uses only three dependent parameters and represents the specific properties of soft biological tissue.

ACKNOWLEDGMENTS

This work was supported in part by the Japan Science and Technology Agency (JST) Precursory Research for Embryonic

Science and Technology (PRESTO), Japan; in part by the Global Centers of Excellence (GCOE) Program and Grants for Excellent Graduate Schools, Japan; and in part by a Grant-in-Aid for Scientific Research from the Ministry of Education, Culture, Sports, Science and Technology (MEXT) (Grant No. 25350577), Japan. We thank an anonymous referee for his/her special effort to help us improve the presentation of the manuscript.

APPENDIX A: REFERENCES TO AUTHORS' OWN WORK

We have conducted studies aimed at developing a rheological model for soft biological tissues with these characteristics, using simple equations and few parameters, that is highly correlated with experimental data [32–39]. The scope of these articles is only to propose a model that is highly correlated with experimental data. The rheological model in this study relies on experimental data obtained from biological tissues. We first give the model equations (A1a) and (A1b):

$$\frac{d^\alpha}{dt^\alpha}(Gx) = f \quad \{x < x_o\}, \tag{A1a}$$

$$\frac{d^\alpha}{dt^\alpha}\{G[1 + a(x - x_o)^2]x\} = f \quad \{x > x_o\}, \tag{A1b}$$

where G is the viscoelastic modulus in the linear region, a is the coefficient determining the change in stiffness in the nonlinear range, and x_o is the threshold of strain between linearity and nonlinearity. The model combines a fractional differential equation with a polynomial expression for stress-strain nonlinearity, which consists of four parameters (G, α, a, x_o).

The model with (A1a) and (A1b) is derived from comprehensive material data obtained from *in vitro* measurements of porcine liver [32–35]. The model with (A1a) and (A1b) was also validated using *in vitro* breast tissue (fibroglandular tissue, fat, muscle) [36,37]. The model (A1a) was partially evaluated in muscle tissue in the linear range [38,39].

The limitations of the above model, proposed by the author in previous studies, compared with the FDEN model, proposed in this article, are as follows. The two parameters (a and x_o) in the model, both parameters representing nonlinear properties, correlate and interfere with one another. In addition, the parameter identification from the experimental data of these two parameters (a and x_o) is complex; specifically, global searching and optimization are required.

The physical law was not explicitly introduced in these articles, while this article explicitly described the laws in soft biological tissue, such as the power law in the time and frequency domains and the exponential law in the stress-strain relationship.

This article also defines a simple identification method fully using the laws. The relationship between fractal geometry (also, holonic systems) and fractional calculus is newly introduced in this article. Moreover, this article newly found that the parameter α (derivative order and also power law exponent) was approximately $\frac{1}{8}$ (=0.125) according to the experimental results of the dynamic viscoelastic tests, as shown in Figs. 3 and 4. This suggests that liver tissue has a complex fractal structure, such as in Fig. 9(c).

APPENDIX B: CALCULATION OF SHEAR STRESS AND STRAIN

In the rheology community, the geometry used here, which comprises two parallel plates in mutual rotation (Fig. 2), is called a plate-plate rheometer. The deformation mode inside it is simple shear. The amount of shear is not uniform throughout the sample since it is proportional to the local distance to the axis of rotation. Although the global action on the rheometer is torsion, the usual denominations for strain and stress are shear strain and shear stress.

Torque T applied to the sample, and the torsional angle θ of the sample, were measured using a plate-plate rheometer (AR-G2 or AR550; TA Instruments, New Castle, DE). From these measurements, the conventional shear strain x and conventional shear stress f were calculated using Eqs. (B1a) and (B1b), respectively:

$$f = \frac{1}{2}\frac{2}{\pi R^3}T, \tag{B1a}$$

$$x = \frac{1}{2}\frac{R}{d}\theta, \tag{B1b}$$

where d and R are the length and radius of the cylinder (see Fig. 2), respectively. The mean stress and strain on the sample (half values of outer stress and strain on the sample) are referred to in the experimental results because they are adequate for consideration of the nonlinear properties. R was 20 mm and d was 5 mm in the experimental setup of this study.

Equations (B1a) and (B1b) are valid only when there is no slip between the sample and the plates. Thus, sandpaper was attached to the top plate and the measurement table to prevent sliding. In a rheometer, correction of the instrument inertia is needed to measure the sample properties. The torque output of the motor comprises the torque required to overcome the instrument inertia and the torque deforming the sample. The torque measurement is influenced by the torque required to accelerate and decelerate the instrument, the oscillating motor shaft and the geometry attached to the shaft. The rheometer used in this study provides an inertia correction function, in which the rheometer collects the inertia of the instrument prior to each measurement as a setup calibration and calculates only stress loaded on the sample using this collected instrument inertia [74]. The effects of instrument inertia become negligible via this correction process in the range of the experimental conditions presented in this article. The instrument inertia correction does not work accurately in some conditions, such as high frequency measurements.

APPENDIX C: CALCULATION OF DYNAMIC VISCOELASTIC TEST

A dynamic viscoelastic test is carried out to measure the data to determine sample properties that depend on the frequency, e.g., compliance (or gain) J, phase ϕ, storage elastic modulus G', and loss elastic modulus G''. If a sinusoidal stress $f(t) = f_o\sin(\omega t)$ is loaded on the sample, a sinusoidal strain $x(t) = x_0\sin(\omega t + \phi)$ that is in phase with the applied strain will result. The method of performing a dynamic viscoelastic test is to apply a sinusoidal strain with amplitude x_o to a sample, over a range of frequencies, and to monitor the strain with amplitude f_o and phase angle ϕ. The properties of the material at a certain angular frequency ω are obtained using the amplitude of the stress f_0, the amplitude of the strain x_o, and phase angle ϕ. Thus, we calculate each value using the following equations:

$$G^{'} = \frac{f_o}{x_o}\cos(\phi), \tag{C1a}$$

$$G^{''} = \frac{f_o}{x_o}\sin(\phi), \tag{C1b}$$

$$J = \frac{x_o}{f_o}. \tag{C1c}$$

The data sets of J, ϕ, G', and G'' are collected at several input angular frequencies ω in the dynamic viscoelastic test. The data sets of (G', G'') at several angular frequencies ω are used to understand mechanical impedance G^* in Sec. III A. The data sets of (J, ϕ) at several angular frequencies ω are used to make the Bode diagram in Sec. III B.

APPENDIX D: POWER LAW IN CREEP TEST WITH HIGH STRESS

The time series data of the creep test exhibited a power law as described in Sec. III C. Equations (1a) and (16) well fit the experimental data at several stress values, and the quantity x_c is well identified. In Sec. III D, the exponential nonlinear model of soft biological tissue is derived from the relationship between x_c and f_c from a series of creep tests under several applied stresses, assuming that Eqs. (1a) and (16) are valid for a single creep test. On the other hand, Eqs. (1a) and (16) and the quantity x_c are theoretically defined only in the linear range at a small strain $x < x_b$, but are not defined in the nonlinear range at large deformations $x > x_b$ in the FDEN model defined by Eqs. (1a) and (16).

This appendix explains that the power law and Eqs. (1a) and (16) for a single creep test are still useful to grasp the quantity x_c in the nonlinear range $x > x_b$, while the quantity α becomes unmeasurable in the nonlinear range $x > x_b$.

The following equation (D1) is equal to (1b); the range is $x > x_b$ in all of the following calculations:

$$t_r^{\alpha}\frac{d^{\alpha}}{dt^{\alpha}}\left(G x_b e^{\frac{x-x_b}{x_b}}\right) = f. \tag{D1}$$

Specifically, Eq. (D1) becomes (D2) if (D1) is solved for the conditions of the creep test. Here, the applied stress is constant f_c:

$$e^{\frac{x-x_b}{x_b}} = \frac{f_c}{G\Gamma(1+\alpha)}\frac{1}{x_b}\left(\frac{t}{t_r}\right)^{\alpha}. \tag{D2}$$

Equation (D3) is derived from (D2) through a division process using reference values x_{bc} and t_b in (D4) at $x = x_b$ for dimensionless quantities:

$$e^{\frac{x-x_b}{x_b}} = \frac{x_c}{x_b}\left(\frac{t}{t_r}\right)^{\alpha}, \tag{D3a}$$

$$\frac{x-x_b}{x_b} = \ln\left[\frac{x_c}{x_{bc}}\left(\frac{t}{t_b}\right)^{\alpha}\right], \tag{D3b}$$

where $\ln(\ldots)$ is the natural logarithm function. The reference values have the following relationship: the reference values are at the boundary position between linear and nonlinear properties in this case,

$$x_{bc} = x_b\left(\frac{t_r}{t_b}\right)^{\alpha}. \tag{D4}$$

The strain x is defined as follows:

$$\begin{aligned} x(t) &= x_b\left\{\ln\left[\frac{x_c}{x_{bc}}\left(\frac{t}{t_b}\right)^{\alpha}\right]+1\right\} \\ &= x_b\left\{\ln\left[\left(\frac{t}{t_b}\right)^{\alpha}\right]+\left[\ln\left(\frac{x_c}{x_{bc}}\right)+1\right]\right\} \\ &= x_b\left\{\ln\left[\left(\frac{t}{t_b}\right)^{\alpha}\right]+\kappa\right\}, \end{aligned} \tag{D5}$$

where κ is defined as follows:

$$\kappa = \ln(x_c/x_{bc}) + 1. \tag{D6}$$

Again, the strain x is defined as follows from (D5):

$$\begin{aligned} x(t) &= x_b\kappa\left\{\frac{1}{\kappa}\ln\left[\left(\frac{t}{t_b}\right)^{\alpha}\right]+1\right\} \\ &= x_b\kappa\left\{\ln\left[\left(\frac{t}{t_b}\right)^{\frac{\alpha}{\kappa}}\right]+1\right\} \\ &= x_b\kappa\left\{\ln\left[\left(\frac{t}{t_b}\right)^{\alpha'}\right]+1\right\}, \end{aligned} \tag{D7}$$

where α' is defined as follows:

$$\alpha' = \frac{\alpha}{\kappa} = \frac{\alpha}{\ln(x_c/x_{bc})+1}. \tag{D8}$$

Equation (D9) is derived from the log-log transformation of (D7):

$$\begin{aligned} \log\left(\frac{x}{x_b}\right) &= \log\left\{\ln\left[\left(\frac{t}{t_b}\right)^{\alpha'}\right]+1\right\} + \log(\kappa) \\ &= \log(t'+1) + \log(\kappa), \end{aligned} \tag{D9}$$

where $\log(\ldots)$ is the common logarithm. t' is defined as $t' = \alpha'\ln(t/t_b)$. The first term on the right side in Eq. (D7) becomes t' by approximation of $\ln(1+t') = t' + O(t'^2)$ around $t' = 0$ using a Taylor series. The condition $t' \ll 1$ is fulfilled in the experimental and theoretical conditions presented in this article. This condition should be checked in the case of a creep test with larger stress or longer term:

$$\begin{aligned} \log(t'+1) &= \frac{1}{\log_{10}e}\ln(1+t') \\ &\approx \frac{1}{\log_{10}e}t' = \frac{1}{\log_{10}e}\ln\left[\left(\frac{t}{t_b}\right)^{\alpha'}\right] \\ &= \log\left[\left(\frac{t}{t_b}\right)^{\alpha'}\right]. \end{aligned} \tag{D10}$$

Then, Eqs. (D11) and (D12) are derived using (D9) and (D10):

$$\log\left(\frac{x}{x_b}\right) = \alpha' \log\left(\frac{t}{t_b}\right) + \log(\kappa), \tag{D11}$$

$$\log\left(\frac{x}{x_c{}'}\right) = \alpha' \log\left(\frac{t}{t_b}\right), \tag{D12}$$

where x_c' is defined as follows:

$$x_c' = \kappa x_b = x_b[\ln(x_c/x_{bc}) + 1]. \tag{D13}$$

Thus, the power law and Eq. (18) are still useful in the nonlinear range of a single creep test. The values of x_c' and α' are identified through parameter identification of the experimental data, the same as in the experiment with the linear range. x_c' is also fulfilled following Eq. (D14) through the expansion of Eq. (D13). Equation (D14) represents time-independent properties for the exponential nonlinear model. Thus, the data from a creep test with high stress, which results in large strain over x_b, are also appropriate for identifying the nonlinear parameters of the FDEN model (D1):

$$e^{\frac{x_c{}' - x_b}{x_b}} = \frac{x_c}{x_{bc}}. \tag{D14}$$

On the other hand, the data from a creep test with high stress, which results in large strain over x_b, are not appropriate for identifying the parameter α of the FDEN model (1): $\alpha' = \alpha/[\ln(x_c/x_{bc}) + 1]$ is identified through the data fitting explained in Sec. III D and Appendix G. Typical experimental results for the relationship between f_c and the α in a series of creep tests are shown in Fig. 5. The identified α with low stress is near $\frac{1}{8}$, an appropriate value from the dynamic viscoelastic test, while the identified α with high stress decreases according to f_c.

APPENDIX E: PARAMETER DEPENDENCY

We modeled the nonlinear properties of soft biological tissue based on these results and considerations, as shown in Eqs. (E1a) and (E1b). The following equations (E1a) and (E1b) describe the static equation of the FDEN model, meaning, in the case of $\alpha = 0$ and $t_r = 1$, assuming that Eqs. (1a) and (2) can hold true in a more general situation for position x and force f, as shown in Sec. III D The equations are the same as Eqs. (19a) and (20):

$$Gx = f \quad \{x < x_b\}, \tag{E1a}$$

$$G_i e^{G_n x} = f \quad \{x > x_b\}, \tag{E1b}$$

where x is strain and f is stress. G is linear stiffness, x_b is the boundary strain, G_n is nonlinear stiffness, G_i is the dependent parameter, and e is Napier's constant. Each parameter should fulfill the condition that the exponential curve (E1b) be tangent to the straight line (E1a) at $x = x_b$. Equations (E2a) and (E2b) are derived from Eqs. (E1a) and (E1b):

$$\frac{df}{dx} = G \quad \{x < x_b\}, \tag{E2a}$$

$$\frac{df}{dx} = G_n(G_i e^{G_n x}) \quad \{x > x_b\}. \tag{E2b}$$

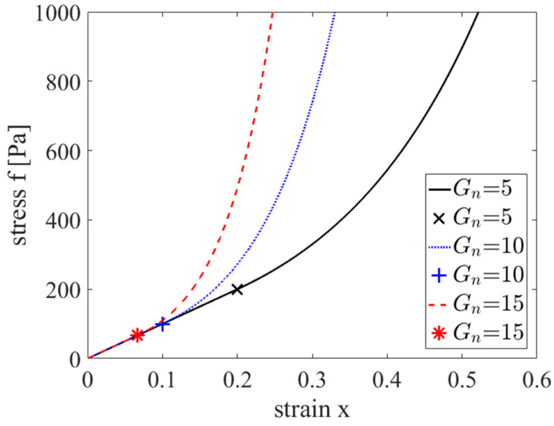

FIG. 11. The stress-strain relationship with several G_n in our model to clarify the meaning of the parameter constraint between G_n and x_b. G was set to 1000 Pa. The line shows stress-strain relationship. The plot shows boundary point.

The continuity of f at x_b may thus be

$$G_i e^{G_n x_b} = G x_b. \tag{E3}$$

Moreover, the continuity of df/dx at x_b should be

$$G_n(G_i e^{G_n x_b}) = G. \tag{E4}$$

By plugging the left-hand side of Eq. (E3) into (E4),

$$G_n x_b = 1. \tag{E5}$$

Then,

$$x_b = \frac{1}{G_n}. \tag{E6}$$

By plugging (E6) into (E4),

$$G_n G_i e = G. \tag{E7}$$

Then,

$$G_i = \frac{G}{G_n e}. \tag{E8}$$

Each parameter may then fulfill the above relationship, particularly (E6) and (E8). The stress-strain relationship with several G_n in our model is described in Fig. 11 to represent the meaning of the parameter constraint between G_n and x_b. Equations (1b) and (19b) are derived by pulling the dependency (E6) and (E8) into Eqs. (2) and (20), respectively.

APPENDIX F: EXTENDED KALMAN FILTER (EKF) FOR DYNAMIC VISCOELASTIC TEST

This appendix shows the methodology used to identify the parameter described in Sec. III A. The model for the dynamic viscoelastic test was as follows from Eqs. (11a) and (11b):

$$\log\left[\frac{G'(\omega)}{G'(\omega_r)}\right] = \alpha \log\left(\frac{\omega}{\omega_r}\right), \tag{F1a}$$

$$\log\left[\frac{G''(\omega)}{G''(\omega_r)}\right] = \alpha \log\left(\frac{\omega}{\omega_r}\right), \tag{F1b}$$

$$G'(\omega_r) = G \cos\left(\frac{\pi}{2}\alpha\right), \tag{F1c}$$

$$G''(\omega_r) = G \sin\left(\frac{\pi}{2}\alpha\right), \tag{F1d}$$

where G', G'', and ω are variables; and α and G are parameters.

We obtained the set of G' and G'' at each value for angular frequency ω from the experiment. We identified the parameter from these data using EKF for system identification (Ref. [75]). The system identification in EKF is generally described as follows:

$$\theta_{k+1} = f(\theta_k, \psi_k), \tag{F2a}$$

$$y_k = g(\theta_k, \zeta_k), \tag{F2b}$$

where $k = 0,1,2,\ldots$ represents the discrete iteration index (number of data sets in this case), θ is the n-dimensional state vector, ψ is the n-dimensional system noise vector, y is the p-dimensional observation vector, ζ is the p-dimensional observation noise vector, and $f(\ldots)$ and $g(\ldots)$ are the nonlinear vector functions. In the theory of state space, (F2a) and (F2b) are known as the system model (or state model) and the observation model, respectively.

The parameter vector is regarded as a state vector in EKF for system identification. Where the state vector (parameter vector) θ is a constant vector and the observation noise vector ζ is a Gaussian white noise with zero mean, (F2a) and (F2b) are represented as

$$\theta_{k+1} = I\theta_k, \tag{F3a}$$

$$y_k = h(\theta_k) + \zeta_k, \tag{F3b}$$

where I is the identity matrix, and $h(\ldots)$ is the nonlinear vector function. In the case of system identification for the dynamic viscoelastic test, the state vector (parameter vector) θ, observation vector y, and the nonlinear vector function $h(\ldots)$ are particularly regarded as follows in the case of $\omega_r = 1$:

$$\theta = \begin{bmatrix} \alpha \\ G \end{bmatrix}, \tag{F4a}$$

$$y = \begin{bmatrix} \log G' \\ \log G'' \end{bmatrix}, \tag{F4b}$$

$$h(\theta) = \begin{Bmatrix} \alpha \log \omega + \log \left[G \cos \left(\frac{\pi}{2}\alpha \right) \right] \\ \alpha \log \omega + \log \left[G \sin \left(\frac{\pi}{2}\alpha \right) \right] \end{Bmatrix}. \tag{F4c}$$

The EKF algorithm [75] using (F4a)–(F4c) was applied to identify the parameter from the data set. It was not necessary to set initial values for each parameter θ_0, meaning that θ_0 was a zero vector.

APPENDIX G: EXTENDED KALMAN FILTER (EKF) FOR NONLINEARITY MEASUREMENT

This appendix shows the methodology used to identify the parameter described in Sec. III D. The model for the nonlinearity measurement is as follows from Eqs. (19a) and (22b):

$$Gx_c = f_c \quad \left\{ x_c < \frac{1}{G_n} \right\}, \tag{G1a}$$

$$G_n x_c = \ln \left(\frac{G_n e}{G} f \right) \quad \left\{ x_c > \frac{1}{G_n} \right\}, \tag{G1b}$$

where f_c and x_c are variables, G and G_n are parameters, and e is Napier's constant. We obtained the set of f_c at each strain x_c from the experiment. We identified the parameter from these series of data sets using EKF for system identification. The algorithm to identify the parameter is the same as in Appendix F, particularly Eqs. (F2a)–(F3b). In the case of system identification for the nonlinearity measurement, the state vector (parameter vector) θ, observation vector y, and nonlinear vector function $h(\ldots)$ are regarded as follows:

$$\theta = \begin{bmatrix} G \\ G_n \end{bmatrix}, \tag{G2a}$$

$$y = \begin{bmatrix} f_c & \left\{ x_c < \frac{1}{G_n} \right\} \\ \ln f_c & \left\{ x_c > \frac{1}{G_n} \right\} \end{bmatrix}, \tag{G2b}$$

$$h(\theta) = \begin{bmatrix} Gx_c & \left\{ x_c < \frac{1}{G_n} \right\} \\ G_n x_c + \ln \left(\frac{G}{G_n e} \right) & \left\{ x_c > \frac{1}{G_n} \right\} \end{bmatrix}. \tag{G2c}$$

The EKF algorithm [75] using (G2a)–(G2c) was applied to identify the parameter from the data set. Each data set affected a single term of the vector, where the upper term for the vectors was updated via low strain data, and the lower term for the vectors was updated via high strain data. Initial values for each parameter θ_0 needed to be explicitly set in the case of the nonlinearity measurement. Therefore, we first approximated the parameters to set the initial values of each parameter θ_0. We used only low strain data (three data sets from minimum strain) for approximation of the parameter G, while we used only high strain data (three data sets from maximum strain) for approximation of parameter G_n. These approximations of the parameters can be identified using LSM: simple linear regression of Eqs. (G1a) and (G1b).

APPENDIX H: RELAXATION TEST

A model equation of stress in relaxation tests can be devised as follows. We assumed that Eq. (1a) is valid for a relaxation test, while nonlinearity was evaluated by a series of relaxation tests under several applied strains. Specifically, Eq. (1a) becomes (H1a) if (1a) is solved for the conditions of the relaxation test. Here, the applied strain is constant x_c. Equation (H1b) is derived from the log-log transformation of (H1a) through the transformation to dimensionless quantities (H1b):

$$f = \frac{Gx_c}{\Gamma(1-\alpha)} \left(\frac{t}{t_r} \right)^{-\alpha} = f_c \left(\frac{t}{t_r} \right)^{-\alpha}, \tag{H1a}$$

$$\log \left(\frac{f}{f_c} \right) = \log \left(\frac{t}{t_r} \right)^{-\alpha} = -\alpha \log \left(\frac{t}{t_r} \right). \tag{H1b}$$

Here, f is stress, t is time, x_c is constant strain, G is linear stiffness at each strain, and $\Gamma(\ldots)$ is the gamma function. f_c is the coefficient determining the stress value as a parameter, which is defined as follows:

$$f_c = \frac{Gx_c}{\Gamma(1-\alpha)}. \tag{H2}$$

The LSM algorithm, linear regression, can be used to identify the parameters of Eq. (H1b) for each sample. We calculated the other independent parameter G via Eq. (H2).

The nonlinear properties of samples can be investigated based on a series of relaxation tests under several applied strains. Specifically, nonlinearity measures the relationship between the constant applied strain x_c and the stress coefficient f_c in the series of relaxation tests under several strains.

APPENDIX I: INDENTATION TEST

A model equation for an indentation test, the reaction force measurement during constant velocity strain change, can be theoretically calculated as follows. It should be noted that the sensitivity of parameter α from the steady state of reaction force f is generally low in experiments with soft biological tissue because the value of the derivative order α was $\frac{1}{8}$ from the experimental results presented in this article. Linear stiffness G and nonlinear stiffness G_n can thus be identified from the reaction force on an indentation test, when the value of parameter α is roughly known. We assumed that Eqs. (1a) and (2), the FDEN model, are valid for the indentation test. We collected time series data for force $f(t)$ on the conditions of the indentation test. Here, the applied strain is $x(t) = v_o t$. Equations (1a)–(2) become identical to static problems such as (I1a)–(I1c) when the fractional integrated stress f' is considered as follows:

$$Gx = f' \quad \{x < 1/G_n\}, \tag{I1a}$$

$$G_n x = \ln\left(\frac{G_n e}{G} f'\right) \quad \{x > 1/G_n\}, \tag{I1b}$$

$$f' = D^{(-\alpha)} f, \tag{I1c}$$

where $D^{(\alpha)}$ refers to αth-order derivative and $D^{(-\alpha)}$ refers to the αth-order integral. The numerical fractional integration, which is necessary in the above calculation, is introduced in various studies (e.g., [76]). Parameters (G and G_n) of Eqs. (I1a) and (I1b) can be identified via the same method introduced in Sec. III D and Appendix G, while we use fractional integrated stress f' on behalf of stress f.

---

[1] Y. Fung, *Biomechanics: Mechanical Properties of Living Tissues* (Springer, Berlin, 1981).
[2] A. Wineman, Math. Mech. Solids **14**, 300 (2009).
[3] Y.-C. Fung, *Biomechanics: Mechanical Properties of Living Tissues* (Springer, Berlin, 2013).
[4] W. Maurel, Y. Wu, N. M. Thalmann, and D. Thalmann, *Biomechanical Models for Soft Tissue Simulation* (Springer, New York, 1998).
[5] H. T. Banks, S. Hu, and Z. R. Kenz, Adv. Appl. Math. Mech. **3**, 1 (2011).
[6] E. Samur, M. Sedef, C. Basdogan, L. Avtan, and O. Duzgun, Med. Image Anal. **11**, 361 (2007).
[7] A. S. Naini, R. V. Patel, and A. Samani, IEEE Trans. Biomed. Eng. **58**, 2852 (2011).
[8] W. Ehlers and B. Markert, J. Biomech. Eng. **123**, 418 (2001).
[9] W. Zhang, H. Y. Chen, and G. S. Kassab, Biomaterials **28**, 3579 (2007).
[10] K. Miller, J. Biomech. **33**, 367 (2000).
[11] K. Miller and K. Chinzei, J. Biomech. **35**, 483 (2002).
[12] J. J. Sarver, P. S. Robinson, and D. M. Elliott, J. Biomech. Eng. **125**, 754 (2003).
[13] D. W. A. Brands, G. W. M. Peters, and P. H. M. Bovendeerd, J. Biomech. **37**, 127 (2004).
[14] C. Chui, E. Kobayashi, X. Chen, T. Hisada, and I. Sakuma, Med. Biol. Eng. Comput. **42**, 787 (2004).
[15] A. E. Kerdok, M. P. Ottensmeyer, and R. D. Howe, J. Biomech. **39**, 2221 (2006).
[16] M. Sedef, E. Samur, and C. Basdogan, in *Proceedings of the 14th Symposium on Haptic Interfaces for Virtual Environment and Teleoperator Systems* (IEEE, Piscataway, NJ, 2006), pp. 201–208.
[17] A. Nava, E. Mazza, M. Furrer, P. Villiger, and W. H. Reinhart, Med. Image Anal. **12**, 203 (2008).
[18] N. Tanaka, M. Higashimori, and M. Kaneko, in *Proceedings of the Annual International Conference of the IEEE for Engineering in Medicine and Biology Society* (IEEE, Piscataway, NJ, 2008), p. 106.
[19] Z. Gao, K. Lister, and J. P. Desai, Ann. Biomed. Eng. **38**, 505 (2010).
[20] S. Zahra, S.-N. Ali, and S. Abbas, Med. Phys. **40**, 051902 (2013).
[21] K. K. Darvish and J. R. Crandall, Med. Eng. Phys. **23**, 633 (2001).
[22] J. Kim, B. K. Tay, N. Stylopoulos, D. W. Rattner, and M. A. Srinivasan, in *Medical Image Computing and Computer Assisted Intervention 2003* (Springer, Berlin, 2003), pp. 206–213.
[23] J.-M. Schwartz, M. Denninger, D. Rancourt, C. Moisan, and D. Laurendeau, Med. Image Anal. **9**, 103 (2005).
[24] J. Kim and M. A. Srinivasan, Med. Image Comput., Comput. Assisted Intervent. **8**, 599 (2005).
[25] H. Liu, D. P. Noonan, Y. H. Zweiri, K. Althoefer, L. D. Seneviratne *et al.*, in *Intelligent Robots and Systems, 2007. IROS 2007, IEEE/RSJ International Conference* (IEEE, Piscataway, NJ, 2007), pp. 208–213.
[26] N. Famaey and J. V. Sloten, Comput. Meth. Biomech. Biomed. Eng. **11**, 351 (2008).
[27] Y. T. Lu, H. X. Zhu, S. Richmond, and J. Middleton, J. Biomech. **43**, 2629 (2010).
[28] A. M. Sims, T. Stait-Gardner, L. Fong, J. W. Morley, W. S. Price, M. Hoffman, A. Simmons, and K. Schindhelm, Biomech. Model. Mechanobiol. **9**, 703 (2010).
[29] S. Marchesseau, T. Heimann, S. Chatelin, R. Willinger, and H. Delingette, Prog. Biophys. Mol. Biol. **103**, 185 (2010).
[30] B. Ahn and J. Kim, Med. Image Anal. **14**, 138 (2010).
[31] E. Basafa and F. Farahmand, Int. J. Comput. Assisted Radiol. Surgery **6**, 297 (2011).
[32] Y. Kobayashi, J. Okamoto, and M. Fujie, in *Proceedings of the 2005 IEEE International Conference on Robotics and Automation* (IEEE, Piscataway, NJ, 2005), p. 1644.
[33] Y. Kobayashi, A. Onishi, T. Hoshi, K. Kawamura, M. Hashizume, and M. G. Fujie, Int. J. Comput. Assisted Radiol. Surgery **4**, 53 (2009).
[34] Y. Kobayashi, A. Kato, H. Watanabe, T. Hoshi, K. Kawamura, and M. G. Fujie, J. Biomech. Sci. Eng. **7**, 177 (2012).
[35] Y. Kobayashi, H. Watanabe, T. Hoshi, K. Kawamura, and M. G. Fujie, in *Soft Tissue Biomechanical Modeling for Computer Assisted Surgery* (Springer, Berlin, 2012), pp. 41–67.

[36] Y. Kobayashi, M. Suzuki, A. Kato, M. Hatano, K. Konishi, M. Hashizume, and M. G. Fujie, IEEE Trans. Robot. **28**, 710 (2012).
[37] M. Tsukune, Y. Kobayashi, T. Miyashita, and G. M. Fujie, Int. J. Comput. Assisted Radiol. Surgery **10**, 593 (2014).
[38] Y. Kobayashi, T. Watanabe, M. Seki, T. Ando, and M. G. Fujie, Adv. Robot. **26**, 1253 (2012).
[39] N. Okamura, M. Tsukune, Y. Kobayashi, and M. G. Fujie, in *Engineering in Medicine and Biology Society, Annual International Conference of the IEEE* (IEEE, Piscataway, NJ, 2014), pp. 6919–6922.
[40] R. Hilfer, *Applications of Fractional Calculus in Physics* (World Scientific, Singapore, 2000).
[41] G. Baumann, in *Fractals in Biology and Medicine*, edited by G. A. Losa, D. Merlini, T. F. Nonnenmacher, and E. R. Weibel (Birkhäuser, Basel, 2005), pp. 287–298.
[42] V. E. Tarasov, Int. J. Mod. Phys. B **27**, 1330005 (2013).
[43] T. Pritz, J. Sound Vib. **195**, 103 (1996).
[44] D. O. Craiem and R. L. Armentano, in *Proceedings of the Annual International Conference of the IEEE for Engineering in Medicine and Biology Society* (IEEE, Piscataway, NJ, 2006), p. 1098.
[45] H. Schiessel and A. Blumen, Macromolecules **28**, 4013 (1995).
[46] M. Caputo and F. Mainardi, Pure Appl. Geophys. **91**, 134 (1971).
[47] M. Caputo and F. Mainardi, R. Nuovo Cimento **1**, 161 (1971).
[48] M. Caputo, J. Acoust. Soc. Am. **56**, 897 (1974).
[49] A. Schmidt and L. Gaul, Nonlinear Dyn. **29**, 37 (2002).
[50] C. Friedrich, Rheol. Acta **30**, 151 (1991).
[51] W. G. Gloeckle and T. F. Nonnenmacher, Macromolecules **24**, 6426 (1991).
[52] N. Heymans and J. C. Bauwens, Rheol. Acta **33**, 210 (1994).
[53] M. Tanter, M. Fink, B. Robert, R. Sinkus, and B. Larrat, in *2006 IEEE Ultrasonics Symposium* (IEEE, Piscataway, NJ, 2006), p. 1033.
[54] B. Suki, A. L. Barabási, and K. R. Lutchen, J. Appl. Physiol. **76**, 2749 (1994).
[55] D. Craiem and R. L. Magin, Phys. Biol. **7**, 13001 (2010).
[56] H. Yuan, E. P. Ingenito, and B. Suki, J. Appl. Physiol. **83**, 1420 (1997).
[57] Q. Chen, B. Suki, and K.-N. An, J. Biomech. Eng. **126**, 666 (2004).
[58] S. E. Duenwald, R. Vanderby, and R. S. Lakes, Ann. Biomed. Eng. **37**, 1131 (2009).
[59] M. Balland, N. Desprat, D. Icard, S. Féréol, A. Asnacios, J. Browaeys, S. Hénon, and F. Gallet, Phys. Rev. E **74**, 021911 (2006).
[60] D. Klatt, S. Papazoglou, J. Braun, and I. Sack, Phys. Med. Biol. **55**, 6445 (2010).
[61] H. Yuan, S. Kononov, F. S. Cavalcante, K. R. Lutchen, E. P. Ingenito, and B. Suki, J. Appl. Physiol. **89**, 3 (2000).
[62] I. Sack, B. Beierbach, J. Wuerfel, D. Klatt, U. Hamhaber, S. Papazoglou, P. Martus, and J. Braun, NeuroImage **46**, 652 (2009).
[63] V. D. Djordjević, J. Jarić, B. Fabry, J. J. Fredberg, and D. Stamenović, Ann. Biomed. Eng. **31**, 692 (2003).
[64] E. Soczkiewicz, Mol. Quantum Acoust. **23**, 397 (2002).
[65] B. Fabry, G. N. Maksym, J. P. Butler, M. Glogauer, D. Navajas, N. A. Taback, E. J. Millet, and J. J. Fredberg, Phys. Rev. E **68**, 041914 (2003).
[66] B. B. Mandelbrot, *The Fractal Geometry of Nature*, Vol. 173 (Macmillan, New York, 1983).
[67] A. Koestler, *The Ghost in the Machine* (Penguin Group, London, 1989).
[68] H. Schiessel and A. Blumen, Fractals **03**, 483 (1995).
[69] H. Schiessel, R. Metzler, A. Blumen, and T. F. Nonnenmacher, J. Phys. A: Math. Gen. **28**, 6567 (1999).
[70] J. F. Kelly and R. J. McGough, J. Acoust. Soc. Am. **126**, 2072 (2009).
[71] R. Kurzweil, *The Law of Accelerating Returns* (Springer, Berlin, 2004).
[72] T. Mizuno, M. Takayasu, and H. Takayasu, Phys. A (Amsterdam) **308**, 411 (2002).
[73] F. Gobeaux, E. Belamie, G. Mosser, P. Davidson, and S. Asnacios, Soft Matter **6**, 3769 (2010).
[74] A. J. Franck, Understanding Instrument Inertia Corrections in Oscillation: TA Instruments, New Castle, DE, 2005.
[75] T. Hoshi, Y. Kobayashi, and M. G. Fujie, in *Proceedings of the 2nd Biennial IEEE/RAS-EMBS International Conference on Biomedical Robotics and Biomechatronics, BioRob 2008* (IEEE, Piscataway, NJ, 2008), p. 730.
[76] C. Ma and Y. Hori, Nonlinear Dyn. **38**, 171 (2004).